EFFECTS OF DUST COMPOSITION ON PARTICLE DEPOSITION IN AN INTERNAL EFFUSION COOLING GEOMETRY

An Undergraduate Thesis

Presented in Partial Fulfillment of the Requirements for

Graduation with Distinction in

the College of Engineering of The Ohio State University

By

Evan Crowe

2019

Thesis Committee:

Dr. Jeffrey Bons, Adviser

Dr. Randall Mathison

ABSTRACT

In this study the effects of dust composition on particle deposition in an effusion cooling geometry were investigated through a series of experiments. Single mineral dusts made from five different minerals, Quartz, Dolomite, Albite, Salt, and Gypsum, were milled to similar size distributions (approx. 0-10µm diameter). These dusts were then used in particle deposition tests on a flat plate effusion hole test article which was heated in a kiln to 1116K and supplied with coolant flow heated to 950K. Percent mass flow reduction per gram and deposit morphology were recorded for each test. Results for the different minerals varied greatly ranging from 7.8% to 160% reduction in mass flow per gram injected, with the albite dust producing the greatest blockage. The different dusts also produced varying shapes of deposits. These five dusts were then combined to form a dust blend with the same mass fractions found in AFRL02, a commercially available test dust, and additional tests were conducted using this dust. Results from the tests using the OSU mixed AFRL02 were compared with an estimated blockage per gram found by taking a weighted average of the blockage per gram for each single mineral dust on a percent volume basis. When tested, the mixed AFRL02 produced a lower blockage per gram than the estimate, indicating that an estimate based on volume fraction alone is not sufficient to predict the deposition of dusts composed of a mixture of minerals.

ACKNOWLEDGMENTS

Firstly I would like to thank my advisor, Dr. Bons. Dr. Bons' guidance, support, and expertise have been very helpful for me in completing this project and learning about how to do research in his lab has been a great experience

I would also like to thank Trent Wolff for helping me get started in the lab, showing me how to run the kiln facilities, and for developing MIPAR recipes and data anlaysis codes I used a bunch this last year. I also appreciate help from Nathan Libertowski with the packing factor data. I'd like to thank everyone in the deposition group as well for help with brainstorming ideas in deposition meetings.

Finally, I would like to extend thanks to all of the members of the lab for providing such a helpful and friendly environment to work in. I think almost everybody has helped me at some point in time over the last year with learning or figuring out how to do something in the lab and I'm grateful to have worked in a lab where everybody is so willing to help

TABLE OF CONTENTS

Page

Abstract ii

Acknowledgments iii

List of Tables vi

List of Figures vii

Chapters:

1. Introduction 1

    1.1 Motivation 1
    1.2 Background 4

2. Experimental Methods 11

    2.1 Dusts Tested 11
    2.2 Milling and Size Analysis 14
    2.3 Experimental Facility and Effusion Test Coupon 19
    2.4 Test Procedure and Conditions 23
    2.5 Post Test Procedure and Data Analysis 24
        2.5.1 Mass Injected Uncertainty Analysis 24

3. Results and Discussion 26

    3.1 Dust Composition vs Size Dependency 32
    3.2 Component Synergy 33
    3.3 Potential Physical Explanations for Test Results 36
        3.3.1 Ideal CoR 36
        3.3.2 Van der Waal Forces 38

3.3.3 Electrostatic Forces 40
3.3.4 Comparing Adhesive Forces 40
3.3.5 Packing Density 42
3.3.6 Melting and Sintering 45

4. Conclusions and Recomendations for Future Work 51

Bibliography 54

LIST OF TABLES

Table **Page**

1.1 ARD Size Ranges Tested in Wolff et al [22] 5

2.1 Dusts Tested 12

2.2 AFRL 02 Composition 13

2.3 QDGS Blend Composition 13

2.4 Microscope-MIPAR Repeatability Statistics where μ is the Mass Mean, σ is the Standard Deviation, and w_d is Calculated Using a Critical Diameter of 3 µm 17

3.1 Mechanical Properties for Tested Materials [21] 37

3.2 Hamaker Constants for Tested Materials 39

3.3 Dielectric Constants for Tested Materials 41

3.4 Comparison of Electrostatic and Van der Waal Forces Calculated for Quartz using Various Separation Distances and Particle Radii (R) . . 41

3.5 Comparison of Adhesive Forces for Various Materials (d=1.2nm, R=2.5(μm) 42

3.6 Dust Melting Points [14][24] 46

LIST OF FIGURES

Figure		Page
1.1	Particulate Mineral Composition from Sites Surveyed in Ref. [7]	3
1.2	Dust Size Distributions in Wolff et al [22]	6
1.3	BPG Results from Wolff et al [22]	8
1.4	Adjusted Blockage per Gram from Wolff et al [22]	9
2.1	50x Microscope Images of Dust Particles. Edges of Images are 250 µm	15
2.2	Milled Dust Size Distributions	16
2.3	AFRL 02 Size Distribution as Measured Via Wet Laser Diffraction alongside ARD Size Distributions as Measured by Coulter Counter	17
2.4	Particle Size Distributions as Measured at Commercial Lab. Note: Salt Maximum Diameter is Approximately 600µm	18
2.5	Test Coupon Geometry (Dimensions in mm)	21
2.6	Experimental Facility	22
3.1	Blockage per Gram Results	27
3.2	Deposit Images at 5X Magnification, Red Oval Indicates the Outline of the Effusion Hole, Scale Bar is 1mm	30
3.3	Deposit Heights (in blue with error bars) Plotted alongside Average BPG (in Red).	31

3.4 BPG_as Calulated for Various Critical Diameters, d_{cr} 33

3.5 Estimated AFRL 02 BPG Compared with Actual AFRL 02 BPGs . . 35

3.6 Impingement Cones 44

3.7 Flow Velocity throughout Effusion Hole. Note: Top of Image Represents Hole Outlet [23] 45

3.8 Temperatures During Sintering Test. Note: Data Logging Software Malfunctioned after 3.25 Hours 48

3.9 Thermocouple Placement inside the Kiln 49

3.10 Images of Dust Piles Pre and Post Bake 50

CHAPTER 1

Introduction

1.1 Motivation

When Helicopters, Aircraft, and other gas turbine powered vehicles operate in a particle laden environment, they are at risk of ingesting airborn particulate, such as ash, dust, or sand, into the engines. This poses a risk to the operation of the gas turbine engine. In the cold section of the engine, particles can collide with and erode compressor blades. In the hot section of the engine, particles will begin to melt and form deposits when they collide with turbine blades and vanes. When this happens, aerodynamic performance of these components is compromised [5].

Cooling air, which in a gas turbine engine is normally supplied by a bleed from the compressor section of the engine, may also become contaminated with ingested particulate. When this happens particulate may deposit in the cooling holes and begin to block the hole. If cooling holes are blocked, then less coolant mass flow is supplied to engine components, which could then reach dangerously high temperatures. Given the potential dangers particle ingestion poses to gas turbine operation, it is important to understand the physical mechanisms that affect deposition so that engines can be designed to mitigate these dangers.

All of these effects have been observed in a variety of full engine deposition tests. Dunn et al. operated a facility that allowed for injecting controlled amounts of dust into full scale gas turbines. It was observed that for engines with a high enough turbine inlet temperature (greater than 2000F) the pressure at the exit of the burner increased rapidly over the period of particle injection. This pressure increase sets up conditions that could eventually lead to a surge. Upon disassembly of the engines used for the tests, large deposits were seen on the turbine inlet guide vanes. The decrease in flow area caused by these deposits was responsible for the increase in pressure according to the authors. Besides the turbine vane deposition, the authors reported other forms of damage to the engine including erosion of the compressor blades and clogging of internal cooling passages [5].

One factor that plays a role in determining how a dust will deposit in an engine is the mineral or chemical composition of the ingested particulate. Natural particulates will vary in composition depending on geographic locations. Volcanic ash samples, for example, varied in chemical composition depending on the specific volcanoes the samples were collected from [17]. Dust too will vary in composition according to geographic location according to a geological survey of dust from different parts of the Middle East (see Figure 1.1) [7]. Furthermore, a survey performed by Smialek et al. indicated that the dust composition at specific size ranges will vary (ie a dust's overall composition may differ from the composition of a sample that was sieved to exclude the larger particles)[16]. This result is particularly interesting when it is considered that many helicopter turboshaft engines are designed with inertial particle separators which will filter out the larger particles from the flow that enters the engine inlet.

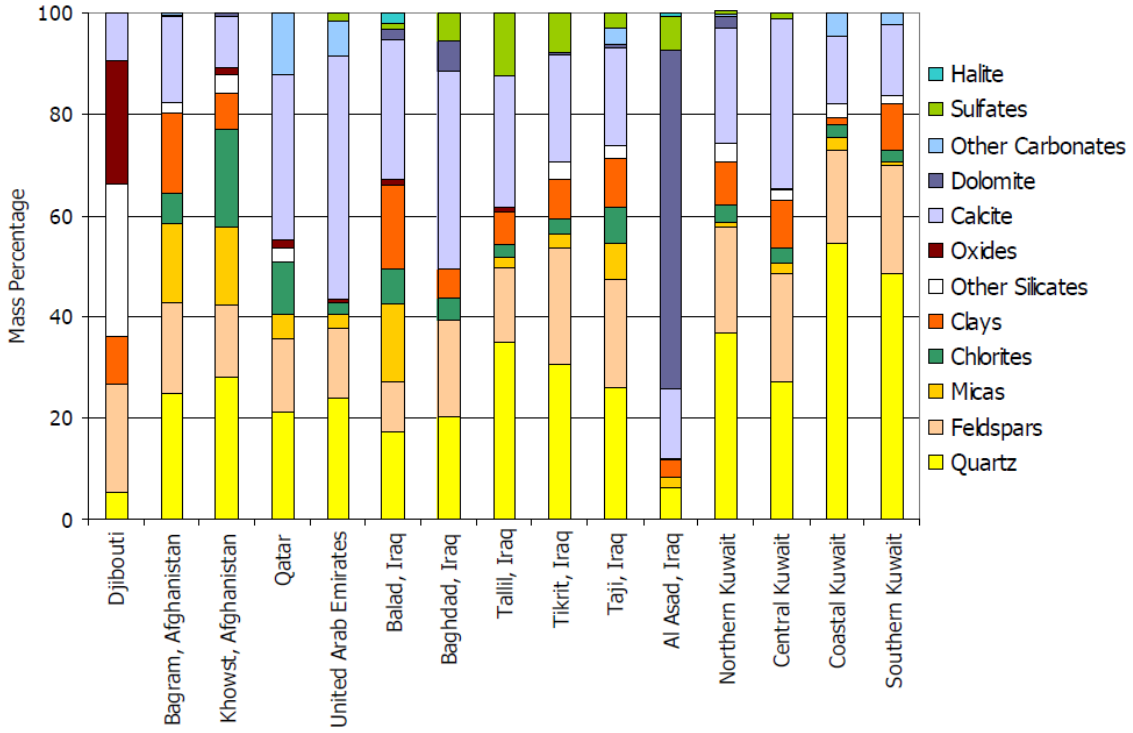

Figure 1.1: Particulate Mineral Composition from Sites Surveyed in Ref. [7]

One implication of differing particulate chemical compositions was explored in a study by Song et al. [17]. The authors performed heating microscope experiments on volcanic ash collected from different sites around the world. In these experiments a sample of ash was heated up to temperatures relevant to the environment found in a gas turbine and the melting behavior was observed. Deformation temperatures, defined as when the cylindrical ash sample begins to lose its shape, were reported. The deformation temperature was considered to be a critical stage in the melting process where the ash would likely stick to a surface and form a deposit. These temperatures were found to vary across ashes collected from different locations, demonstrating how material differences can affect properties relevant to deposition. The authors were able

to correlate the differing deformation temperatures to a material dependent property, namely the ratio of acidic to basic oxides found in the ash $R_{a/b}$. This quantity varied from ash to ash and did a good job of predicting an ash's melting behavior.

While the Song et al. study did not exactly simulate an engine environment, other deposition studies using real engine hardware have reported that particulate composition will affect deposition rates. Webb et al. performed deposition experiments in a facility where turbine vanes were subjected to ash laden air at similar temperatures to those found in an engine. Four different types of coal ash were used as the particulate [19]. Four turbine vanes were subjected to ash laden air at a variety of flow temperatures. It was found that as the temperature increased so did the thickness of the deposits. This temperature dependence has been observed in numerous deposition studies including the previously discussed full engine test [5]. A particularly interesting result of the work by Webb et al. in the context of this thesis is how the deposition characteristics varied with different types of ash. It was found that the different ashes had varying temperature at which the ash particles began to stick to the vanes and also formed deposits of varying thickness. This result demonstrates the importance of particulate chemistry in determining how it deposits.

1.2 Background

So far mostly deposition in the external gas path of the engine has been discussed, but deposition will also affect internal cooling channels. Several studies have investigated deposition in these geometries. One such study by Wolff et al. provided the motivation for this thesis and so it will be summarized here[22].

Table 1.1: ARD Size Ranges Tested in Wolff et al [22]

Dust Type
0-3 μm
0-5 μm
0-10 (I) μm
0-10 (II) μm
5-10 μm
10-20 μm

This study used an accelerated deposition facility to investigate deposition using a test article with an array of effusion holes. The test plate was fixed to a fixture that was located inside a modified pottery kiln. The test conditions (temperature, geometry, and pressure ratio across the effusion holes) were kept constant while the dust that was used varied from test to test. Specifically, the dust size distribution was varied. All tests used Arizona Road Dust (ARD). This dust is commonly used for gas turbine dust ingestion tests and comes in a variety of sizes. The dusts ranged from 0-3 μm to 10-20 μm. All the size ranges tested are listed in Table 1.1 and the size distributions as measured by the vendor using a Coulter Counter are shown on Figure 1.2. This plot shows the cumulative mass distribution. The y-axis indicates the mass percent of dust particles below a certain diameter and the x-axis is the particle diameter on a log scale. A diameter of $3\mu m$ is highlighted because it was determined to be a critical diameter for deposition. This will be further explained in the following paragraphs.

The aim of this study was to develop an understanding of how small differences in a particle size distribution affect deposition. Looking at Figure 1.2 one notes that

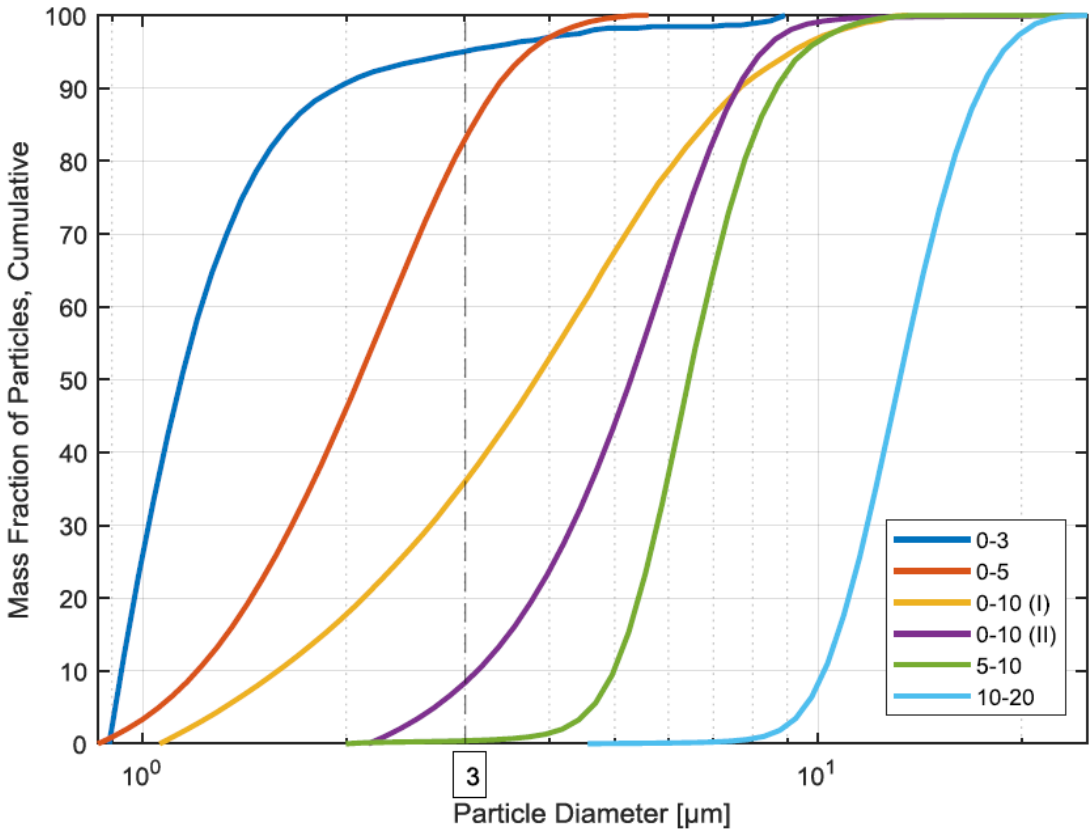

Figure 1.2: Dust Size Distributions in Wolff et al [22]

there are two different size distributions labeled 0-10 μm. They are labeled (I) and (II) to differentiate them. These two dusts represent two different batches of dust in the 0-10 size range. Despite having mostly all particles in the same size range, the size distributions are different: 0-10 (I) has a larger fraction of particles skewed towards the smaller end of the 0-10 range.

The results of Wolff et al. are shown in Figure 1.3. The results are reported in terms of BPG, blockage per gram. This quantity is a way to describe a dust's ability to cause cooling hole blockage where a higher BPG would mean it takes less mass of dust to block the cooling holes compared to a dust with a lower BPG. Comparing the BPG results with the dust size ranges, a trend is evident: the dusts with a smaller size range block cooling holes in this geometry more effectively. Between the two 0-10 dusts, the dust with more of its mass skewed to the small end of the size range has a higher BPG.

The authors wondered if there was a certain particle size that contributed the most to deposition. The hypothesis was that a certain critical particle diameter, d_{cr}, could be identified such that knowledge of the mass fraction of dust below this particle diameter could be used to predict deposition between dust types. The authors found that a critical diameter did exist, and was about 3.25 µm. Figure 1.4 shows the analysis that was completed to determine this critical diameter. An adjusted BPG was calculated (BPG_a) according to Equation 1.1. In this equation, w_d is the mass fraction of particles less than the critical diameter (d_{cr}). If the hypothesis is true that particle size is a dominant factor in deposition, then as the mass fraction of particles below that diameter increases, BPG should increase monotonically.Additionally, when BPG is divided by w_d, then BPG_a will be constant across all size ranges. Figure 1.4

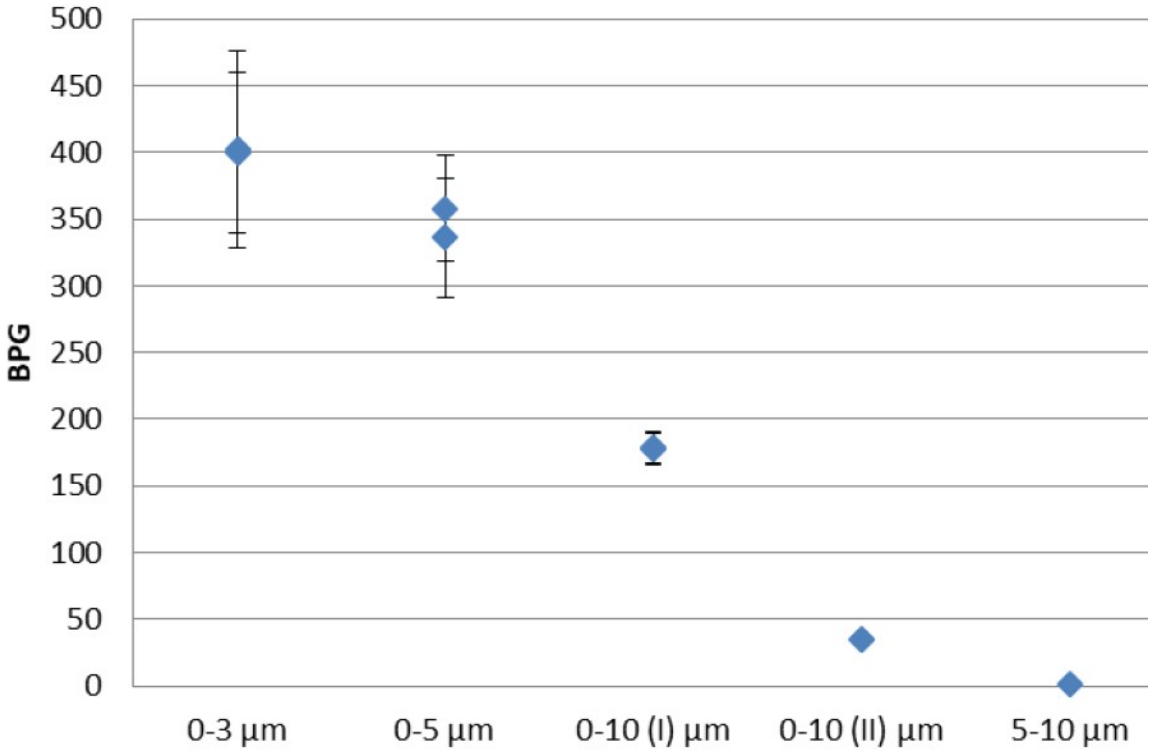

Figure 1.3: BPG Results from Wolff et al [22]

shows that when w_d is set to 3 or 3.5 microns, BPG_a is nearly the same for each dust, indicating that a critical diameter of 3.25 microns likely exists.

$$BPG_a = BPG/w_d \tag{1.1}$$

The main conclusion from Wolff et al. is that smaller sized dust particles contribute the most to blocking the cooling holes in the effusion cooling geometry that was used for the study. Specifically, it appears as if it is particles less than 3.25 µm that are primarily responsible for blocking the effusion holes. This prompts the question: why are the smaller particles depositing more? Is it due to the particles'

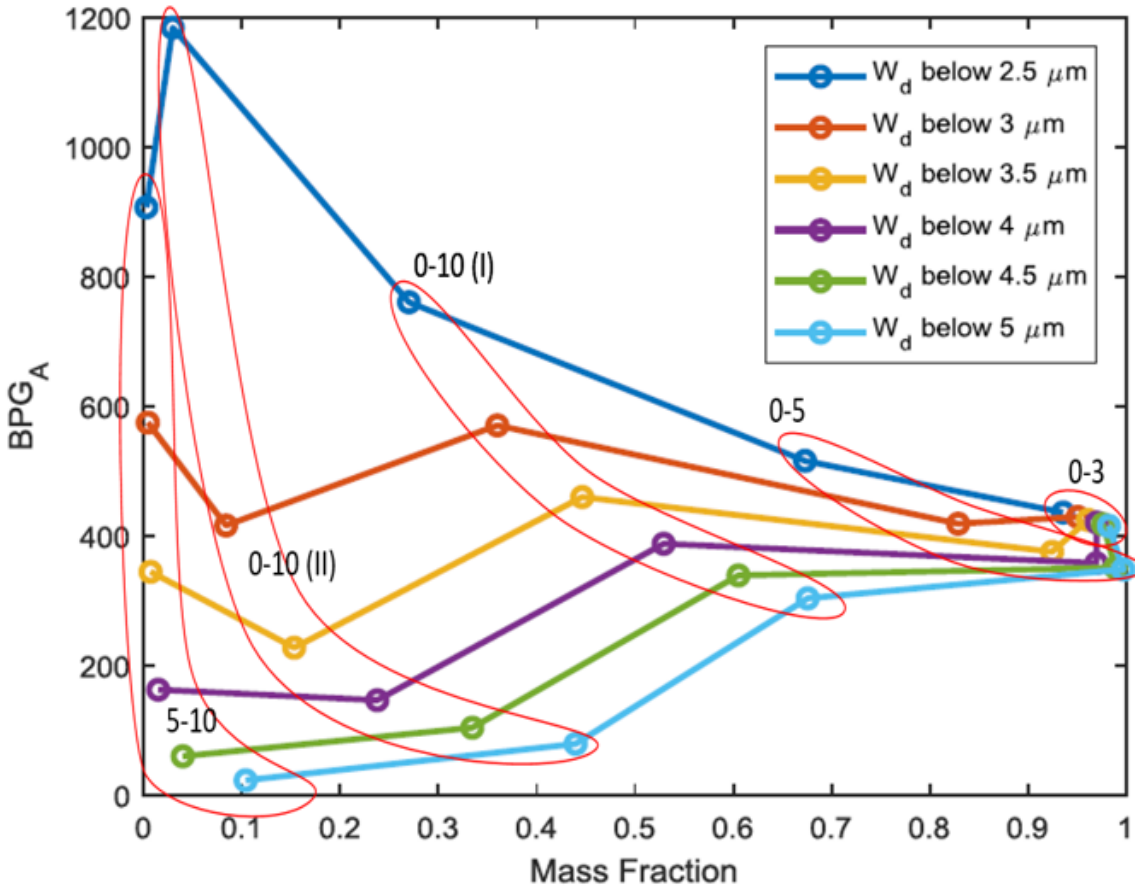

Figure 1.4: Adjusted Blockage per Gram from Wolff et al [22]

small size alone? An alternative explanation could be that the stickiest components of ARD are found in a higher concentration among the dust particles less than 3.25 µm in diameter. ARD is a dust collected from natural sources and then carefully processed to obtain the desired size distributions. It seems likely that dusts and dirts will have different constituent ratios at different size ranges (like was seen in reference [16]). These questions provide the motivation for studying the effects of composition on deposition in internal cooling geometries.

The purpose of this work is to investigate the effects of dust composition of particle deposition independent of size distribution, in order to better understand the interactions between different constituents that affect cooling hole blockage. To accomplish this, deposition tests will be performed using an accelerated deposition facility. Five single mineral dusts will be tested and then they will be combined in the same mass fractions as they are found in AFRL 02, a common deposition test dust that will be described in Chapter 2. More tests will be completed with the AFRL 02 created by mixing these dusts, as well as other versions of AFRL 02 described in Chapter 2. The results of these tests will then be used to judge material dependent factors that affect deposition in internal cooling geometries

This thesis is divided into four chapters. Chapter 2 will describe the methods used to complete this study including methods for size analysis, a description of the test facility, as well as a description of the test procedure and data analysis. Chapter 3 will describe the results of the test campaign as well as discuss the physical context for the test results. Chapter 4 will discuss conclusions that may be made as well as suggestions for future work.

CHAPTER 2

Experimental Methods

2.1 Dusts Tested

The dusts used in this study are listed in Table 2.1. Five single mineral dusts were used: albite, dolomite, quartz, gypsum, and salt. These dusts were on hand in larger size ranges (40-80 µm for most dusts). To test the composition related effects independent of size distribution, it is important to control the size distribution. Additionally, it is desirable to have the dusts be a similar size distribution of those in Wolff et al., namely 0-10 µm ARD [22]. To reach this size distribution, the dusts were milled to a 0-10 µm size range.

These dusts were chosen because they are the ingredients to a synthetic dust blend that was created for use in gas turbine deposition tests, AFRL 02 [13]. AFRL 02 consists of these minerals in the mass ratios shown in Table 2.2. Aplite is listed as an ingredient in AFRL 02, although it was not readily available. Aplite is a type of rock that consists of feldspar and quartz. Albite is a specific type of feldspar and was used in place of aplite in this study.

Three varieties of AFRL 02 were tested. One variety was purchased from a dust supplier, PTI and milled to the appropriate size distribution. An unmilled version

Table 2.1: Dusts Tested

Dust	Approx. Size Range	Chemical Formula
Quartz	0-10 µm	SiO_2
Dolomite	0-10 µm	$CaMg(CO_3)_2$
Albite	0-10 µm	$NaAlSi_3O_8$
Salt	0-10 µm	$NaCl$
Gypsum	0-10 µm	$CaSo_4 * 2H_2O$
OSU-mixed AFRL 02	0-10 µm	N/A
milled PTI AFRL 02	0-10 µm	N/A
QDGS Blend	0-10 µm	N/A
unmilled AFRL 02	0-60 µm	N/A

of this dust was also tested. The milled single mineral dusts were also combined in the ratios listed in Table 2.2 to create a third variety of AFRL 02. This 'OSU-mixed' variety is unique because all components are present in the same size distribution while for milled PTI AFRL 02 the size distribution was not controlled on a component basis- only the overall size distribution was measured. Thus the size distribution will likely differ between constituents due to them milling at different rates inside the mixture. One more dust mixture was also tested. This mixture contains only quartz, gypsum, dolomite, and salt, and thus was denoted as the QDGS Blend. It excludes albite, which was found to be a high blocking dust. Its composition is shown in Table 2.3.

Table 2.2: AFRL 02 Composition

Component	Mass %
Quartz	34
Gypsum	30
Aplite	17
Dolomite	14
Halite (Salt)	5

Table 2.3: QDGS Blend Composition

Component	Mass %
Quartz	38.25
Gypsum	17.125
Aplite	0
Dolomite	18.25
Halite (Salt)	9.25

2.2 Milling and Size Analysis

To mill the dusts from the larger size distributions down to around 0-10 microns, dust was placed into a container with zirconium balls and acetone. Acetone was chosen so that none of the dusts would dissolve in the liquid and to help mix the dust in with the zirconium balls. This container was then placed on rollers and rolled for 72-120 hours. Intermittently, the milling was stopped to check the size distribution of the dust.

Size distributions were measured optically, by collecting microscope images at 50x magnification. Microscope slides were prepared by dispersing a small amount of dust on a slide, and then squishing the dust between that and another microscope slide. Microscope images are then processed using MIPAR^{TM}, an image processing software, to identify the particles in the images and measure their diameters. Figure 2.1 shows microscope images of the particles before and after MIPAR^{TM} processing. These measurements were used to create a cumulative size distribution that may be plotted along side ARD 0-5 and 0-10 dust size distributions in order to make a comparison in Figure 2.2.

The supplier provided dust size distributions as measured by a Coulter Counter. This device measures particle sizes while they are suspended in an electrolytic solution. This suspension is then passed through microchannels and the particle size can be determined by measuring the change in impedance of the electrolytic fluid as the particles pass through the microchannels. One factor that affects the accuracy of any particle size analysis is the tendency for small particles to clump together. Depending on how well these agglomerations are dispersed prior to measurement, some will be counted as single particles and the overall distribution will appear to be

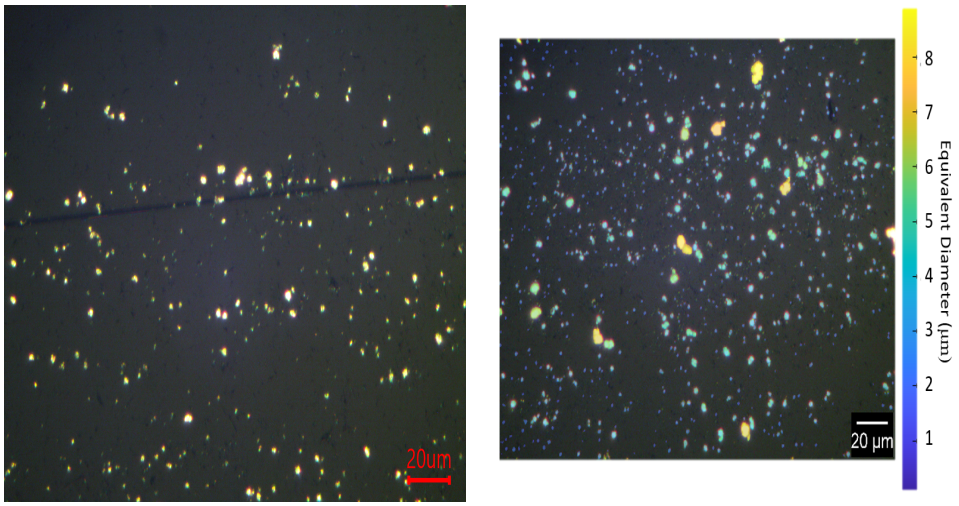

(a) Microscope Image before MIPAR Processing

(b) Particulate Image after MIPAR Processing and Measurement. Colors Indicate Various Particle Diameters

Figure 2.1: 50x Microscope Images of Dust Particles. Edges of Images are 250 µm

larger than it actually is. Different methods of particle sizing will disperse the clumps to different extents, so it can be misleading to compare particle size distributions that were measured using different methods. Therefore, it was necessary to measure the ARD dusts using the microscope-MIPAR method as well so that a better comparison may be made. The ARD distributions shown on Figure 2.2 were measured by the microscope-MIPAR method, which is why they extend beyond 5 and 10 µm respectively.

Unmilled AFRL 02 was also tested. The size distribution of this dust was measured via wet laser diffraction by the dust supplier. This size distribution is plotted alongside the distributions of ARD as measured via Coulter Counter in Figure 2.3.

The measurement process for the milled dusts was performed multiple times to verify repeatability. For some dusts, the repeatability was very good, while for other

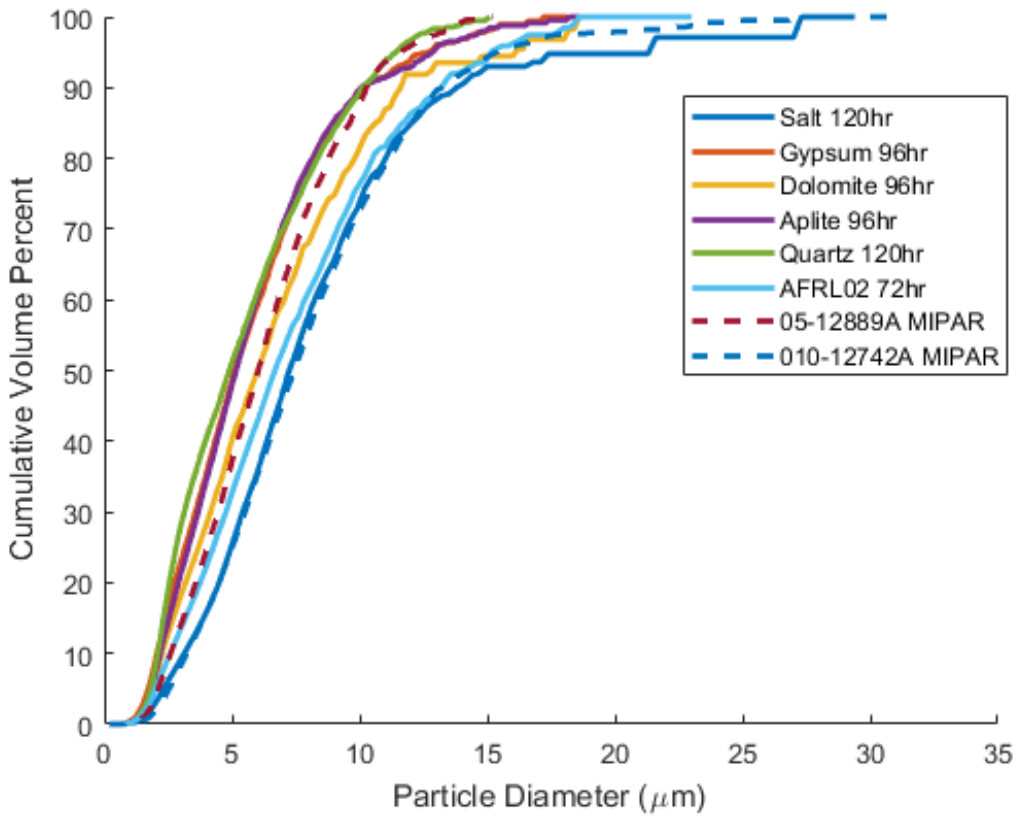

Figure 2.2: Milled Dust Size Distributions

dusts, like salt and quartz, the measurements varied slightly from measurement to measurement. Table 2.4 shows statistics from the microscope-MIPAR measurements so that the repeatability of the measurements can be compared.

The dusts were also sent out to a commercial particle sizing lab with the hope to obtain a more accurate size distribution. The result of this analysis is shown in Figure 2.4. This lab used a third method of particle size analysis, dry laser diffraction. This method suspends the dust in swirling air to disperse the individual particles. The particle laden air is then passed through a laser and the way the laser is refracted can

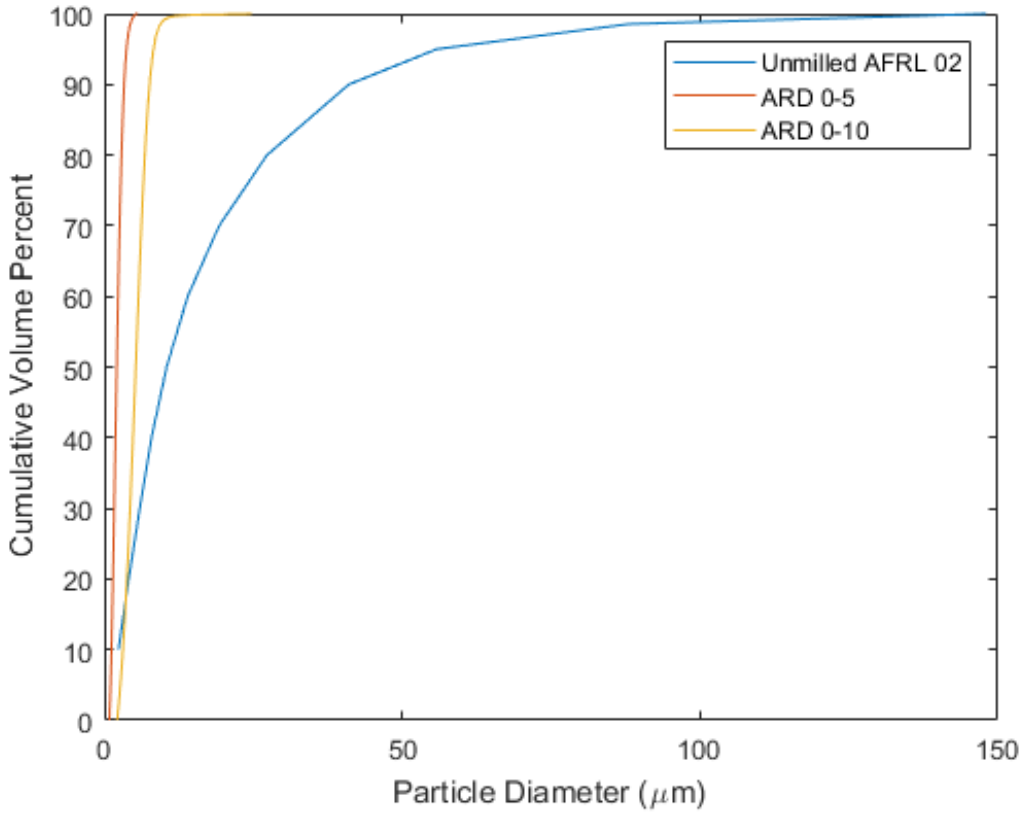

Figure 2.3: AFRL 02 Size Distribution as Measured Via Wet Laser Diffraction alongside ARD Size Distributions as Measured by Coulter Counter

Table 2.4: Microscope-MIPAR Repeatability Statistics where μ is the Mass Mean, σ is the Standard Deviation, and w_d is Calculated Using a Critical Diameter of 3 µm

Gypsum			Salt			Dolomite			Quartz			Albite			AFRL 02		
µ	σ	w_d	µ	σ	w_d	µ	σ	w_d	µ	σ	w_d	µ	σ	w_d	µ	σ	w_d
5.79	1.24	0.242	8.56	1.82	0.111	6.84	1.39	0.221	7.11	1.29	0.256	5.84	1.3	0.225	6.73	1.33	0.203
5.66	1.31	0.249	7.12	1.65	0.144	7.07	1.29	0.250	6.99	1.43	0.206	5.70	1.32	0.252	7.50	1.58	0.159
5.59	1.33	0.206	5.87	1.43	0.234	6.54	1.32	0.215	5.54	1.18	0.296	5.48	1.25	0.243	6.84	1.42	0.202

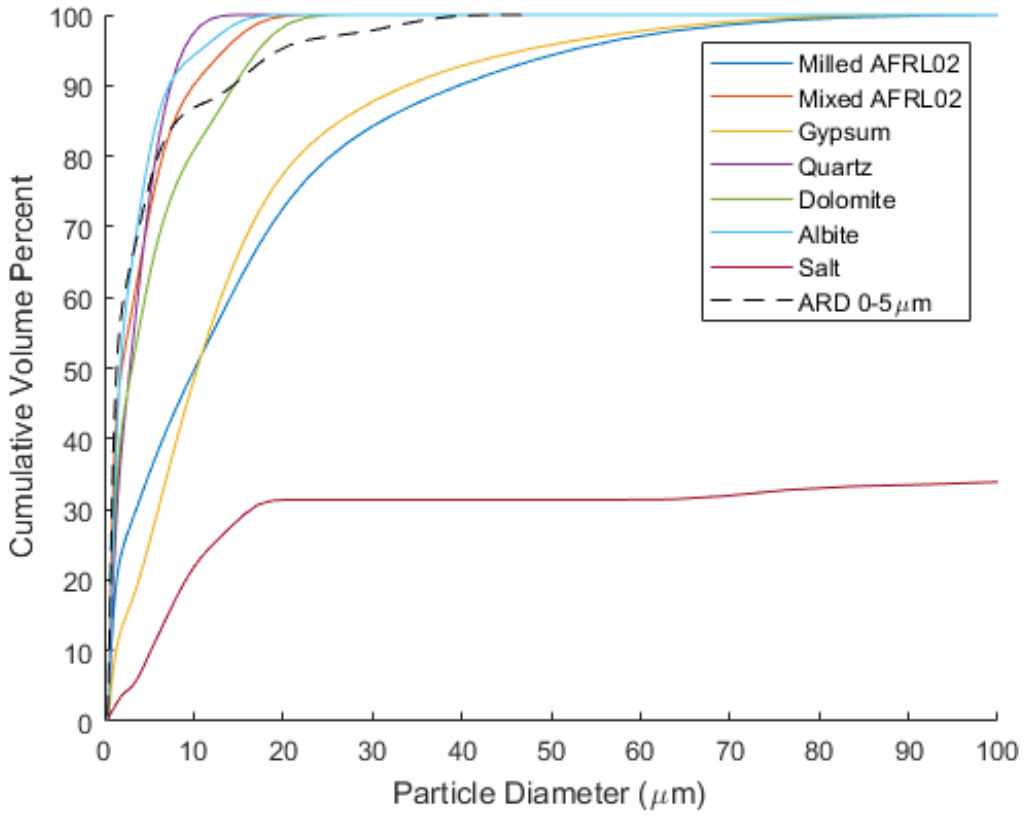

Figure 2.4: Particle Size Distributions as Measured at Commercial Lab. Note: Salt Maximum Diameter is Approximately 600µm

be used to determine the particle size. As shown in Figure 2.4 the size distributions vary dramatically between the two sizing methods. Furthermore, certain dusts appear to have very large size distributions. This is surprising because all dusts were milled for about the same time. As discussed in the previous paragraph, clumping is a problem when measuring particle size. It is thought that the dry laser diffraction method did not do a very good job dispersing the particles evenly across the different dusts. This can be seen by observing that the salt size distribution extends well beyond 100 microns and that the ARD 0-5 dust extends well beyond 5 microns. Compared to an optical method of particle size measurement, the extent to which the particles have agglomerated is difficult to know when using the laser diffraction method. Using an optical method of particle sizing, the degree of dispersion may be judged before measuring. After collecting microscope images, if a large amount of clumping is observed, that image may be excluded. Because of this, it is thought that the microscope-MIPAR method of size analysis is the more credible measurement in this case.

2.3 Experimental Facility and Effusion Test Coupon

Testing was completed on an accelerated deposition facility shown if Figure 2.6. In this facility, an effusion test plate is supplied with particle laden coolant air. The test coupon geometry is shown in Figure 2.5. The coolant air is introduced parallel to the effusion plate before making a 150 degree turn to exit the hole.

The test coupon is mounted to a fixture located inside a kiln which is turned on during a test to heat the coupon. The coolant is heated using a 6 kW heater that is located inline with the air supply. In the test section, pressure is monitored using

a 0-1 PSID pressure transducer with an accuracy of 0.08 %. Coolant temperature is measured using a K-type thermocouple with an accuracy of 3K. Because the thermocouple is located inside a duct whose walls are hotter than the coolant flow, the thermocouple will be heated by radiation and conduction from the walls of the test fixture and the measured temperature will be higher than the flow temperature. To account for this, the measured temperature is corrected using the method described by West and Westwater [20]. The plate temperature is measured via IR camera which was calibrated using a thermocouple spot welded to the test plate.

Mass flow is supplied to the fixture by a 0-100 SLPM mass flow controller upstream of the inline heater. This mass flow controller has an accuracy of 0.8% reading and 0.2% full scale. When the test starts, the mass flow is about 90 SLPM which corresponds to about 1% accuracy during a test. Dust is supplied to the facility from a pressurized feedbox. Inside the feedbox, there is a conveyor belt that is controlled remotely to deliver the dust at a specified rate. The dust falls off the conveyor belt into the funnel and drop tube where it enters the main coolant flow. A small amount of mass flow (1 SLPM) is provided to the feedbox to prevent the main coolant flow from entering.

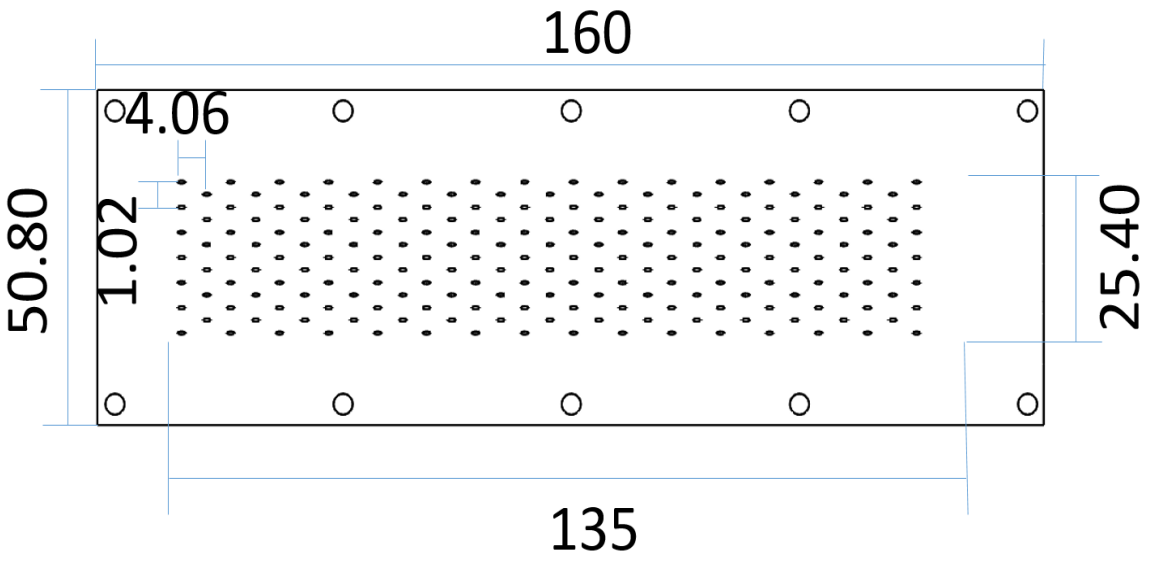

(a) Effusion Plate

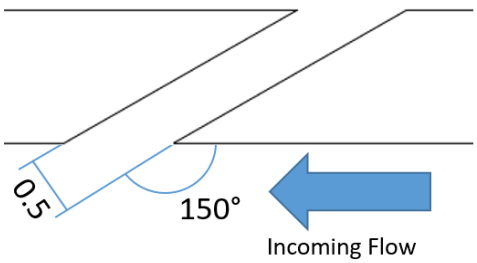

(b) Effusion Hole Cross Section

Figure 2.5: Test Coupon Geometry (Dimensions in mm)

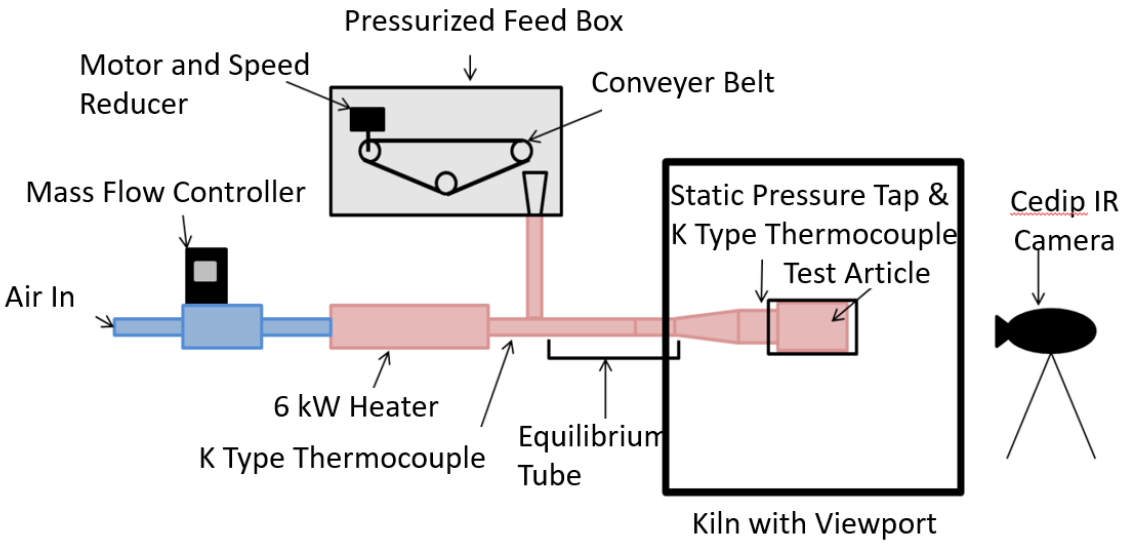

Figure 2.6: Experimental Facility

2.4 Test Procedure and Conditions

When starting a test, enough coolant mass flow is supplied to achieve a pressure ratio of 1.03 across the test plate. The 6 kW heater is turned on and adjusted so that the coolant flow reaches a temperature of 950K. The test plate is heated by the kiln and the set point of the kiln is adjusted until the external surface temperature of the test plate is brought to 1116K.

Before each test, approximately 0.5-0.7g of dust is loaded evenly onto the conveyor belt. Once the test facility is heated up and steady state thermal conditions have been reached, dust delivery begins. The conveyor belt moves at a rate slow enough so that the volumetric concentration of dust particles in the coolant is on the order of about 10^{-9}, which is low enough to consider the flow dilute. In this regime of particle concentration, there is one-way coupling between the fluid and the solid particles which means that the fluid determines particle trajectories while the particles don't have a significant impact on the flow field. At higher concentrations, the particles could influence the flow field as well or, at very high concentration, even bump into other particles. These regimes are discussed in more detail by Elghobashi [6].

During the test the pressure inside the test section will increase as the effusion holes begin to block. When the pressure increases mass flow is reduced automatically via a control loop programmed in LABVIEW to maintain constant pressure 1.03 ratio. Once the mass flow is reduced by 25 % from the starting mass flow, the test is ended. For some dusts that exhibited very minimal blockage 25% mass flow reduction was never achieved and so the test was ended after all the dust was delivered.

2.5 Post Test Procedure and Data Analysis

After the test is completed any dust remaining on the belt is collected and weighed in order to determine the total amount of dust injected during the test. To quantify how aggressively a dust blocks during a test, blockage per gram, BPG, is calculated by dividing the percent mass flow reduction (MFR) by the mass of dust injected into the facility during the test (m_{inj}) as shown in Equation 2.1.

$$BPG = \frac{MFR}{m_{inj}} \tag{2.1}$$

Comparing BPGs from tests using different dust's allows for a comparison of a dust's ability to block effusion holes. If during a test a lower mass of dust is required to achieve the same reduction in coolant mass flow, then the BPG calculated for that test will be higher which indicates that the dust used for that test blocked aggressively.

After the kiln has cooled, the test plate is removed from the fixture and the deposits on the upstream side of the plate are imaged via microscope.

2.5.1 Mass Injected Uncertainty Analysis

An uncertainty analysis was performed for the BPG quantity following the partial derivative method described by Moffat [12]. The measurement for the (m_{inj}) term in Equation 2.1 comes from a scale with a precision of 0.0001g. The uncertainty will likely be higher than the uncertainty associated with the scale, however, due to the process of transferring the dust onto the belt and having it travel down the funnel into the coolant flow. It is likely that some dust will stick to the conveyor belt, funnel, or walls of the drop tube. To determine the amount of dust lost in this process, the drop tube, which is the vertical section of tubing shown in Figure 2.6, was decoupled from

the rest of the facility. Dust was weighed and then placed on the conveyor belt. The conveyor belt was then turned on, and dust was sent down the funnel and collected in a cup at the end of the drop tube. This collected dust was then weighed. This test was repeated several times and it was found that the difference between the two measurements was approximately 2.5%. This indicates that the m_{inj} term will be on average 2.5% less than the reported value and this uncertainty was used when calculating uncertainty of BPG.

CHAPTER 3

Results and Discussion

Most dusts were tested at least three times. For salt, dolomite, and unmilled AFRL 02 only two tests were performed since the repeatability was good. Due to time contraints, only one test was performed for the QDGS blend. Figure 3.1 shows the blockage test results.

The BPGs varied quite dramatically for the five single mineral dusts. Albite produced the highest blockage with BPGs around 175 while dolomite and salt both blocked minimally with BPGs around 10. The mixed dusts also showed different blocking behaviors. OSU-mixed AFRL 02 had a lower BPG than the milled PTI AFRL 02. This result demonstrates the importance of constituent size distributions since the size distribution of the individual constituents between these two dusts likely differs. The unmilled AFRL 02 had the lowest blockage among the AFRL 02 dusts. This result makes sense when the size range of unmilled AFRL 02 is considered- its maximum particle diameter ranges to about 60 microns.

The QDGS blend had a lower BPG than the OSU-mixed AFRL 02. Although it may be hard to make a conclusion with only one data point for the QDGS Blend, this result was expected since this dust has the same constituents as OSU-mixed AFRL 02 except for the highest blocking dust, albite. The QDGS blend does have a higher

percentage of salt than normal AFRL 02 however. At the temperatures in these tests, salt may melt, which was seen in sintering tests described in Section 3.3.6. In a mixture, if one constituent melts, then it could bind to other particles and increased their deposition rate, so, it's possible that if the fraction of salt was reduced to that of AFRL 02, the BPG would have been even lower.

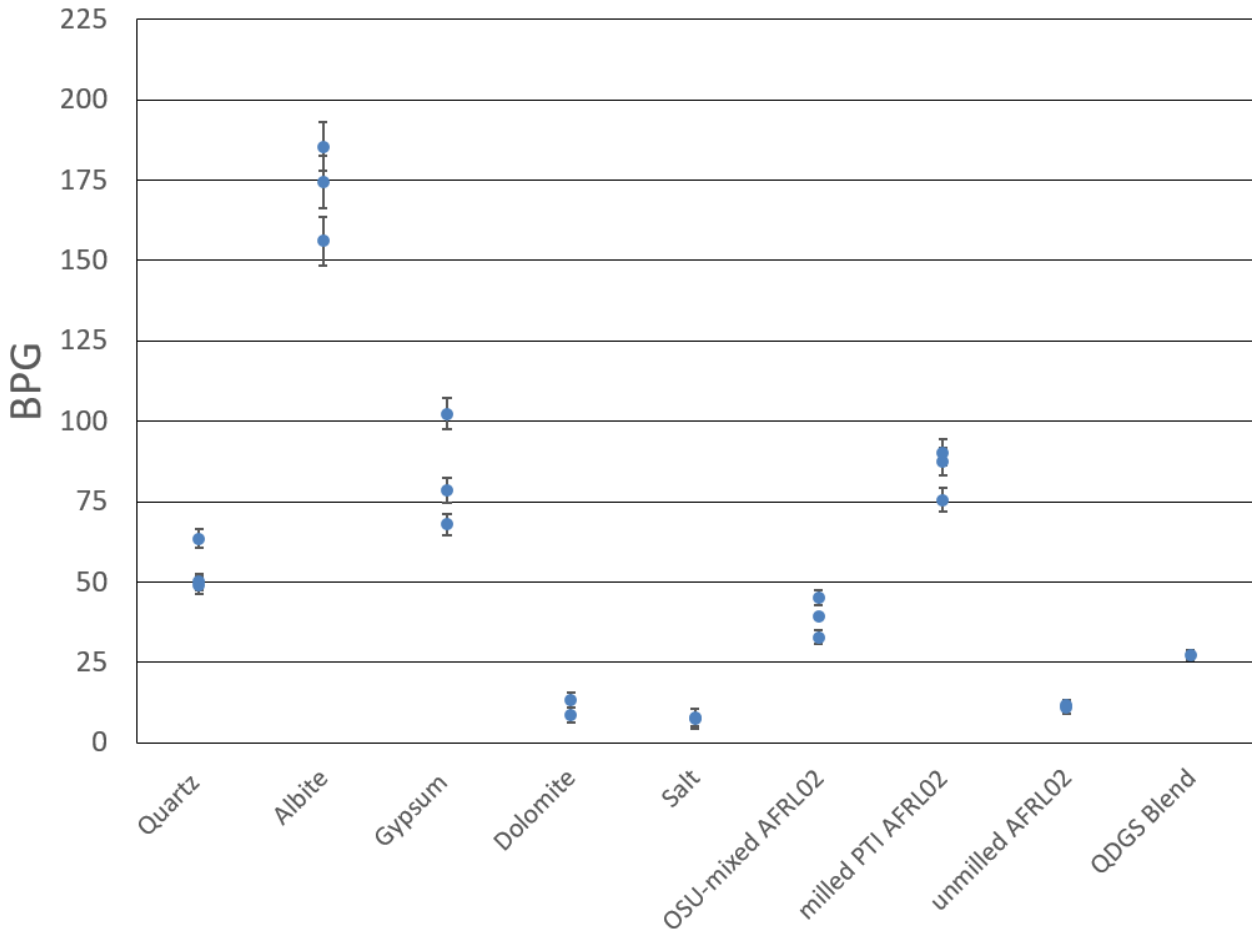

Figure 3.1: Blockage per Gram Results

In addition to the different dusts having different BPGs, the deposit morphology also varied. Images of the deposits can be seen in Figure 3.2. These deposits formed on the upstream or 'cool' side of the effusion plate. In these images the red oval indicates a nominal outline of the effusion hole. Certain dusts formed 'V' shaped deposits which extended into the hole (albite and gypsum) while other dusts formed amphitheater shaped deposits that sat on the downstream end of the effusion hole (quartz and dolomite). The salt deposits were small and only seen inside the effusion hole. The deposits from the mixed dust had small deposits on the sides of the effusion holes that extended from the main deposit. This feature was interesting because it was not seen in any single mineral deposit. In particular it is interesting to compare the OSU-mixed AFRL 02 deposit to the deposits of the single mineral dusts. The OSU-mixed AFRL 02 is a dust that contains only the dusts that were tested as single mineral dusts. The fact that the deposits of these dusts change when they are mixed together indicates that there is some interaction that occurs when these single mineral dusts are combined that affects how they deposit.

Deposit heights were also measured after each test using a microscope with a graduated focus knob marked every 2 microns. The results are shown in Figure 3.3. The uncertainty of this measurement was found to be quite large, approximately 25% and was found by comparing the height measured by the microscope to the height measured by a high precision 3d scanner, which was acquired after the testing was completed.

There are a few interesting observation to be made from Figures 3.3 and 3.2. For most dusts the BPG and deposit heights increased or decreased together. Intuitively this might make sense- a dust that deposits more would have a higher BPG and a

larger deposit. But when it comes to blocking effusion holes the location and shape of the deposit are also important. Dolomite had a very low BPG compared to other dusts but it had one of the tallest deposits. An explanation for this could be its higher density- dolomite particles may be less likely to make the 150 degree turn through the effusion hole. Additionally, the amphitheater shaped deposit formed by the dolomite particles could raise the discharge coefficient through the hole. This would allow particles to travel faster through the hole and would lead to less sticking in the hole as particles impact at a higher velocity. The deposit could also be changing the streamlines through the hole and cause particles to impact at a shallower angle which also would reduce the likelihood of sticking. Albite on the other hand did not have a deposit that extended far beyond the surface of the effusion plate and thus did not have a tall deposit. Despite this the BPG was much higher for albite than it was for dolomite.

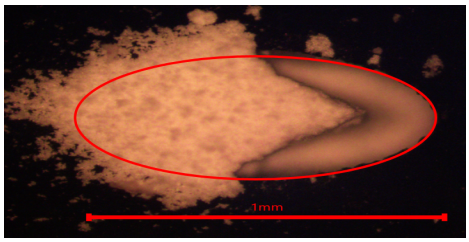

(a) Gypsum

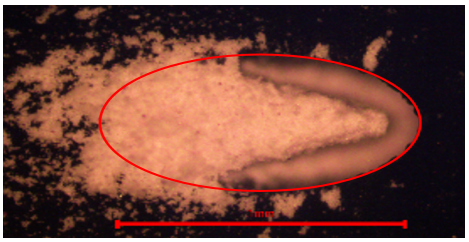

(b) Albite

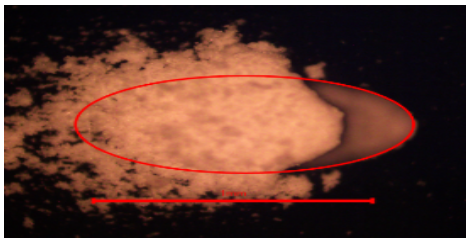

(c) Quartz

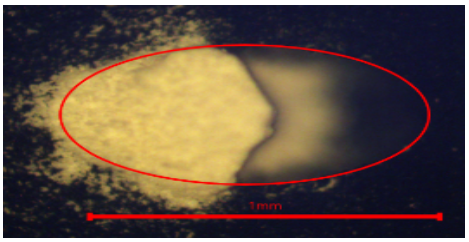

(d) Dolomite

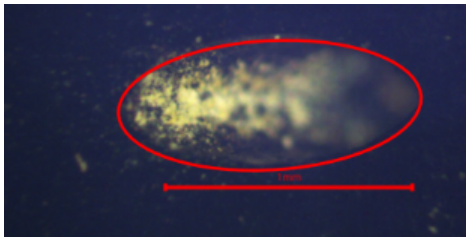

(e) Salt

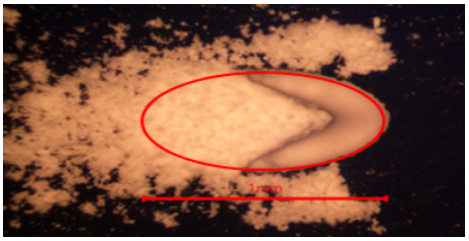

(f) Milled PTI AFRL 02

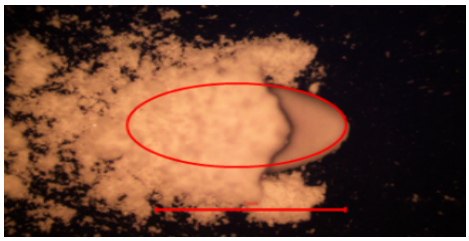

(g) OSU-Mixed AFRL 02

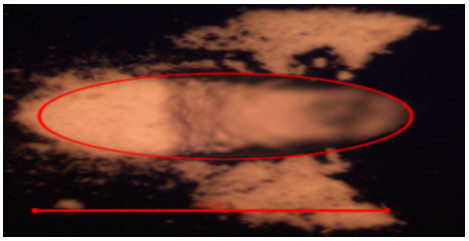

(h) Unmilled AFRL 02

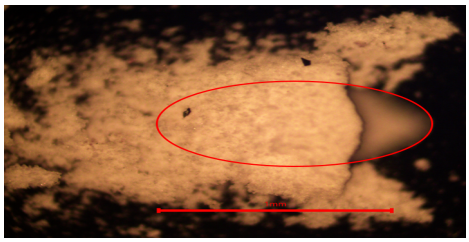

(i) QDGS Blend

Figure 3.2: Deposit Images at 5X Magnification, Red Oval Indicates the Outline of the Effusion Hole, Scale Bar is 1mm

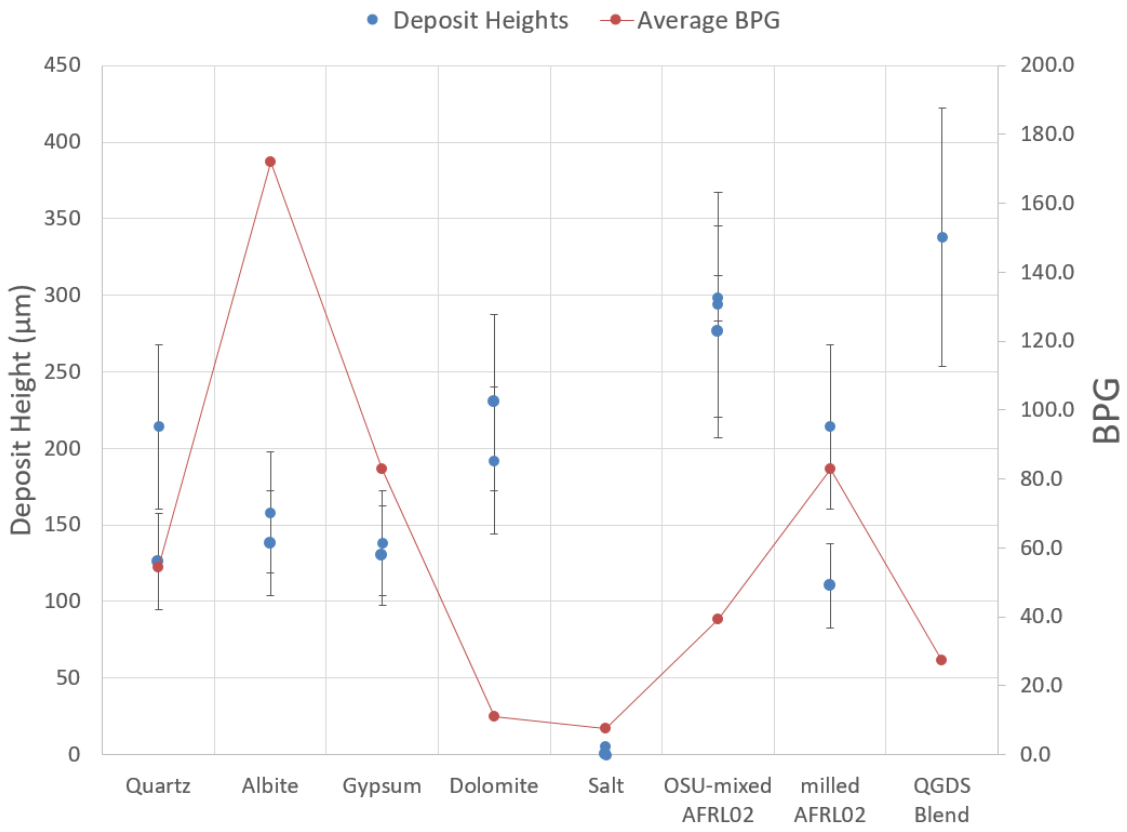

Figure 3.3: Deposit Heights (in blue with error bars) Plotted alongside Average BPG (in Red).

3.1 Dust Composition vs Size Dependency

The aim of this study was to isolate material dependent effects from size dependent effects. Looking at Figure 2.2 however, there is some variance still in the size distributions. It is important to make sure that these differences in size distributions were not a significant parameter influencing the test results. To verify that the differences in BPGs were decided by differences in dust composition and not size distribution, the same analysis that was done in Wolff et al. ([22]) may be done for the present work using the dust size distributions seen in Figure 2.2. As discussed in Section 2 the dust size distributions used for this study were not measured using a Coulter Counter as was used in Wolff et al. Measuring particle sizes optically has the tendency to skew the measurement towards a higher distribution as the particles clump. Because of this, the same critical diameter, d_{cr} should not be used and if a critical diameter exists it will likely be larger than the one found for ARD in Wolff et al.

Adjusted BPGs were calculated for a variety of critical diameters according to Equation 1.1. The results are shown in Figure 3.4. For no critical diameter do all of the BPGs collapse into a straight line when normalized by w_d. In fact, for every diameter the dust with the highest BPG_a is albite, followed by gypsum and quartz, then salt and dolomite. The lines connecting all the BPG_as are nearly vertical. The fact that they don't collapse into a horizontal line likely indicates a true material dependence of these test results. This contrasts with Figure 1.4 where a constant BPG_a is found for each dust by normalizing the BPGs by the mass fraction of particles below the derived critical diameter.

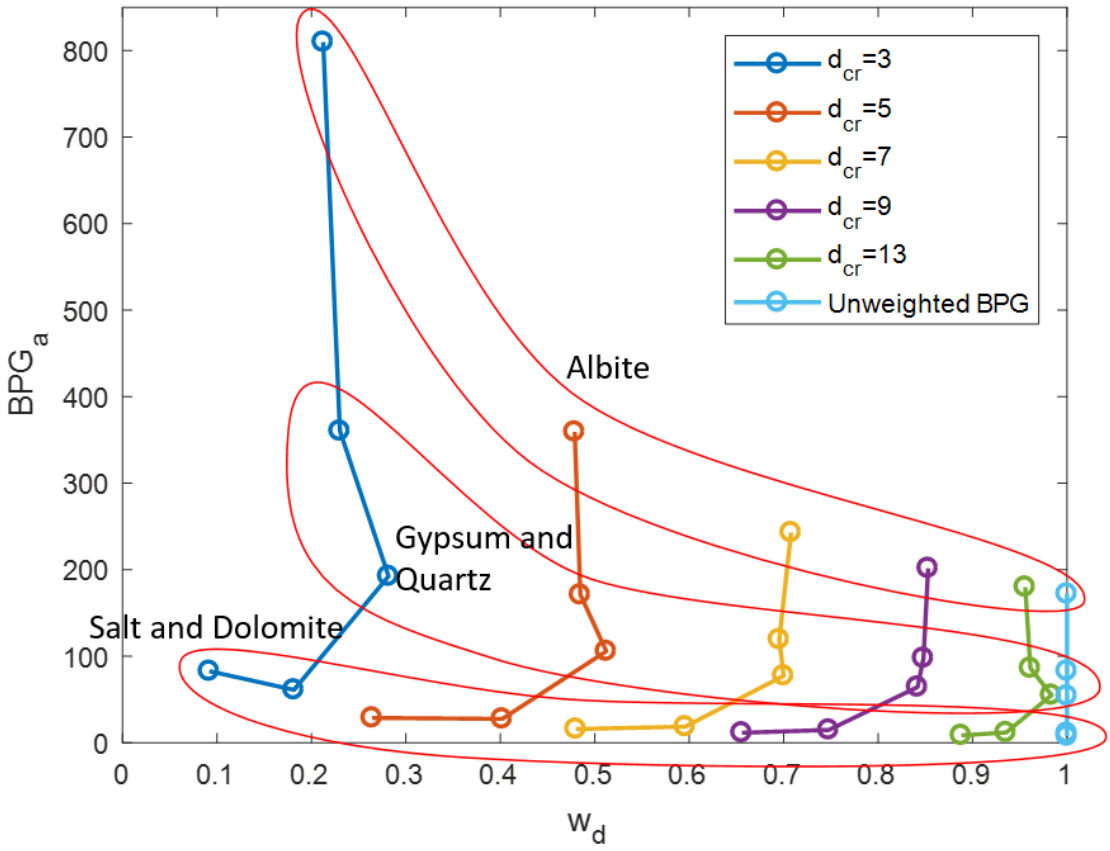

Figure 3.4: BPG_as Calulated for Various Critical Diameters, d_{cr}

3.2 Component Synergy

Because both single mineral dusts as well as dusts that were made by mixing these single mineral dusts were tested, it is interesting to consider whether any interactions may occur between the individual constituents when a mixed dust is tested. Using the BPG results from the single mineral dusts (Figure 3.1) and the mass fractions of the single consitutents found in AFRL 02 as shown in Table 2.1, an estimated BPG was calculated by taking a weighted average of the BPGs of the constituent dusts.

If each dust in a mixture deposits independently and doesn't interact with the other components of the mixture, then it would be expected that the estimate would be fairly accurate. Observing from Figure 3.5 this is not the case. This indicates there is some interaction between the minerals present in the mixture that reduces the BPG. While this analysis does not identify the specific interaction a few potential interactions may be considered. Some dusts have taller deposits as seen in Figure 3.2. The OSU-mixed AFRL 02 dust also showed fairly tall deposits. One possibility could be that the dusts that formed large deposits, like dolomite and quartz, still create large deposits even when they are in a mixture like OSU-mixed AFRL 02. This shape of deposit could act as a chute to funnel air through the hole with a higher discharge coefficient, and thus a higher velocity, decreasing the tendency for stickier materials like albite to stick inside the hole. Another possibility could be that substances that don't stick as well as albite could have eroded the deposits formed by particles that were sticking. Testing different mixtures of dusts that exclude certain materials could shed some light on the specifics of the interactions.

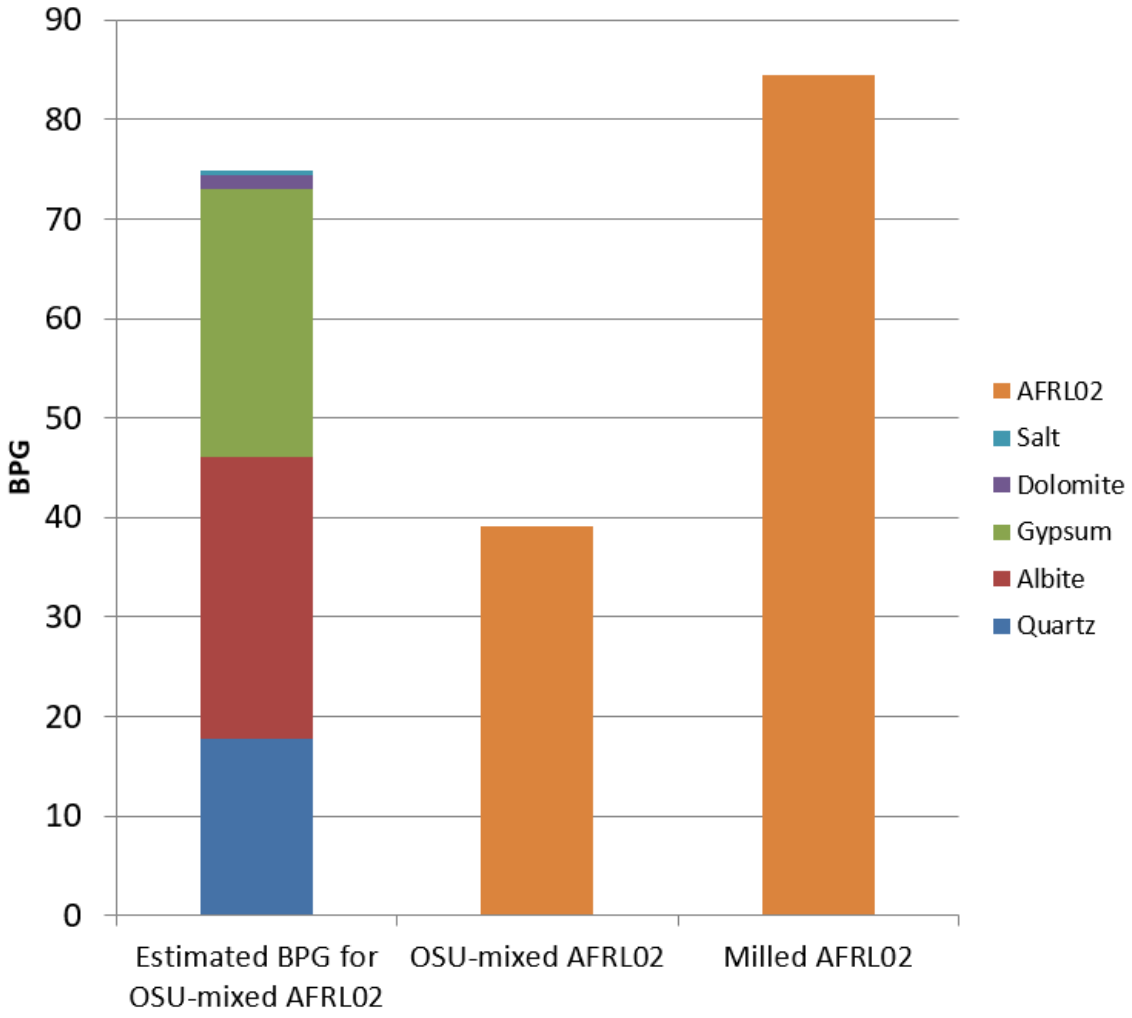

Figure 3.5: Estimated AFRL 02 BPG Compared with Actual AFRL 02 BPGs

3.3 Potential Physical Explanations for Test Results

An obvious question that arises when considering the test results shown in Figure 3.1 is: what is the determining factor that is causing the varying BPGs across the single mineral dusts? The primary variable that was changed across the different dusts was the dust composition, and as discussed in the previous section the discrepancy in size distribution doesn't seem to have determined the test results, so it is thought that differing material properties is responsible for the different blocking behaviors of the different dusts. The following sections will present different material dependent properties of the dusts and consideration of the role they may have played in determining the different BPGs of the dusts.

3.3.1 Ideal CoR

The OSU Deposition model is a physics based model for predicting particle deposition in gas turbine engines [2]. It provides a simple framework that may be used to predict whether a particle that impacts a surface sticks or rebounds if the material properties of the surface and particle are known. The model provides equations for calculating a coefficient of restitution (CoR) for a particle. If the CoR is 0 then the particle sticks. The 'ideal' CoR , $\mathrm{CoR_{ni}}$, is defined as the CoR where adhesion and fluid shear are not considered and only elastic-plastic deformation are taken into account. According to the OSU deposition model, $\mathrm{CoR_{ni}}$ only depends on the mechanical properties of the surface and particle such as the yield stress, σ_{y}, particle density, ρ, and the effective Young's Modulus between the particle and the surface, $\mathrm{E_{eff}}$, defined by Equation 3.1, where ν_p and ν_s represent the particle and surface Poisson's Ratio and E_p and E_s represent the particle and surface Young's Modulus

Table 3.1: Mechanical Properties for Tested Materials [21]

Material	ρ (kg/m^3)	E_{eff} (GPa)	a (Pa/(m/s))	ν	σ at 50 m/s (MPa)	$\sqrt{\frac{{\sigma_y}^2}{\rho E}}$	Average BPG
Quartz	2650	95.3	3.02	0.073	151	9.50	54.2
Albite	2630	70.3	2.86	0.315	53	10.52	172
Gypsum	2350	45.7	1.06	0.33	143	5.12	82.9
Salt	2160	30.1	0.91	0.26	133	5.64	7.6
Dolomite	2865	116.2	2.66	0.295	45.5	7.29	11.6

respectively.

$$E_{eff} = (\frac{1-{\nu_p}^2}{E_p} + \frac{1-{\nu_s}^2}{E_s})^{-1} \tag{3.1}$$

Assuming these material properties are known, then the ideal CoR is given by Equation 3.2.

$$CoR_{ni} = \sqrt{\frac{{\sigma_y}^2}{\rho E}}\frac{1}{V_{n1}} \tag{3.2}$$

The V_{n1} term is the inbound particle velocity normal to the surface. According to Equation 3.2 a higher value for the quantity $\sqrt{\frac{{\sigma_y}^2}{\rho E}}$ will correspond to a higher CoR, higher rebound velocity, and less likelihood of depositing. The material properties for the single mineral dusts tested in this study were found by Whitaker and Bons and are listed in Table 3.1 [21]. The authors account for rate of strain effects by allowing the yield stress to vary with particle velocity according to Equation 3.3 where 'a' represents the yield stress coefficient. In Table 3.1, V_{n1} was taken to be 50 m/s.

$$\sigma_y = (aV_1) * 1e6 \tag{3.3}$$

Judging from Table 3.1, comparing ideal CoRs does not explain the test results. Assuming all particles are following similar trajectories into the hole then albite should

have the highest rebound velocity ($\sqrt{\frac{{\sigma_y}^2}{\rho E}}$) according to the ideal CoR calculation, and thus be least likely to deposit. This is the opposite of what was seen in the test results where albite blocked most effectively. The validity of the assumption that the particles are following similar trajectories may be affected by the differing particle densities however. Denser particles will not follow the flow streamlines as closely for a given particle diameter which would affect where they impact inside the hole.

Besides plastic deformation, adhesion will also absorb incoming particles' kinetic energy and act to keep particles stuck to surfaces. At smaller ranges of particle sizes, like the size range of particles used in this study, these forces will become much more influential on the deposition process [4][2] Adhesive forces that will act on the particles include capillary, electrostatic, and van der Waal forces. Because the dusts were baked after milling and stored in airtight containers with desiccant packets, it is thought that capillary forces will be minimized. This leaves electrostatic and van der Waal forces. Both of these forces are material dependent so an analysis of these forces may provide an explanation for the varying BPGs.

3.3.2 Van der Waal Forces

Van der Waal Forces may calculated between two objects of the same material if the Hamaker constant, A, is known for the material. The specific expression will differ from geometry to geometry but the van der Waal forces may be calculated between two particles of equal size using Equation 3.4 below where A is the Hamaker constant, R is the particle radius, and d is the separation distance[9].

$$F_{VdW} = \frac{AR}{12d^2} \tag{3.4}$$

The Lifshitz theory of van der Waal forces describes how A can be calculated for a macroscopic particle. Calculation of A requires knowledge of spectral data for a material such as the refractive index of the material as a function of light wavelength. Hough and White summarized the calculation of A using this data [8]. Bergström evaluated several simplified methods for calculating A and also tabulated A for a variety of materials [1]. Looking at Equation 3.4, the van der Waal force will depend directly on A if the geometry between two particles are constant. As such, A may be used to compare relative strengths of van der Waal forces for different materials. Several Hamaker constants for materials used in this study were found in the literature and are tabulated in Table 3.2. Unfortunately Hamaker constants were not available for albite and gypsum nor was the optical data required to calculate the Hamaker constants. Judging from the Hamaker constants that were available it doesn't seem that van der Waal forces alone explain the test results. For quartz, dolomite, and salt, the BPG and A both increase together (Figure 3.1), but the BPG for quartz was 4-5 times larger than for salt and dolomite while the value for A was not that much greater than the values for A for salt and dolomite.

Table 3.2: Hamaker Constants for Tested Materials

Material	A (10^{-20} J)	Average BPG	Reference
Quartz	8.64	54.2	[1]
Gypsum	N/A	82.9	N/A
Albite	N/A	172	N/A
Dolomite	7.34	11.1	[11]
Salt	6.43	7.6	[1]

3.3.3 Electrostatic Forces

Another adhesive force that acts on particles is electrostatic force. Any time particles are transported pneumatically through tubing they will collide with the walls and each other and likely develop an electric charge. If the charge of a particle is known then it is simple to calculate the electrostatic force between it and another particle or surface. The exact charge is difficult to know however. Lee and Fan developed an expression shown in Equation 3.5 for electrostatic force by considering the maximum charge a particle can hold before causing an electric breakdown of the surrounding air to neutralize the charge [11]. This expression was developed for perfectly spherical particles and is a function of particle surface area, S, and the dialectric constant, ϵ_r. It should be noted that the nonspherical nature of the particles used in this study as well as varying air properties may affect the validity of this equation.

$$F_{es,max} = 79.2S\frac{3\epsilon_r}{\epsilon_r + 2} \tag{3.5}$$

From Equation 3.5, a higher dielectric constant should correspond to a higher electrostatic force, and thus greater deposition. The dielectric constants for the materials tested are listed in Table 3.3 and it can be seen that there is no clear correlation dielectric constants and BPGs.

3.3.4 Comparing Adhesive Forces

Using Equations 3.4 and 3.5 a rough comparison may be made to see if either force dominatesr. Values for A and ϵ_r are given for quartz, and salt by Bergström [1] while these values are given by Lee and Fan [11] but the separation distance, d, is still unknown. Separation distance is usually on the order of nanometers and will likely

Table 3.3: Dielectric Constants for Tested Materials

Material	ϵ_r	Average BPG	Reference
Quartz	4.29	54.2	[1]
Gypsum	5-11.5	82.9	[18]
Albite	5.4-7.1	172	[18]
Dolomite	7.34	11.1	[11]
Salt	5.9	7.6	[1]

Table 3.4: Comparison of Electrostatic and Van der Waal Forces Calculated for Quartz using Various Separation Distances and Particle Radii (R)

R(μm)	S(m^2)	d(m)	F_{es}(N)	F_{vdW}(N)
2.5	7.85e-11	1.16e-9	1.27e-8	1.34e-8
2.5	7.85e-11	5.29e-10	1.27e-8	6.44e-8
5	3.14e-10	1.16e-9	5.09e-8	2.68e-8
5	3.14e-10	5.29e-10	5.09e-8	1.29e-7

vary across different materials as seen by Salazar-Banda et al. [15]. In the study by Salazar-Banda et al., separation distances were determined experimentally using a centrifuge for two different materials with known Hamaker constants. The authors were able to correlate the rotation rate of the centrifuge at the moment a particle was ejected from the centrifuge to the van der Waal force. This then allowed a calculation of the separation distance. Separation distance decreased slightly as particle diameter decreased, but remained fairly constant across the size range tested. In Table 3.4, separation distances were taken from the smallest diameter tested by Salazar-Banda et al., 13µm, for both materials tested in the study. Judging from Table 3.4, both

Table 3.5: Comparison of Adhesive Forces for Various Materials (d=1.2nm, R=2.5(μm)

Material	F_{es} (N)	F_{vdW}(N)	Average BPG
Quartz	1.27e-8	1.34E-8	54.2
Dolomite	1.47e-8	1.14e-8	11.1
Salt	1.39e-8	9.96e-9	7.6

forces are of a similar value at this size range and should both be considered when assessing the effect of adhesion forces.

The same comparison between adhesive forces can also be made for dolomite and salt, the other two materials for which the Hamaker constant is known. Table 3.5 shows this comparison. For the other two materials, the forces are still similar in magnitude. Which force is greater depends on the specific material however.

3.3.5 Packing Density

Another factor that can affect deposition in effusion holes is a dust's packing density. When dust begins to deposit, if one dust forms less dense deposits, then the effusion hole will become blocked faster by a smaller amount of dust. One way to determine how densely a dust deposits is to measure the packing factor (PF). This quantity is defined in Equation 3.6 as the density of the deposit, ρ_{dep} divided by the density of the material, ρ_{mat}.

$$PF = \frac{\rho_{dep}}{\rho_{mat}} \tag{3.6}$$

To try and measure packing factors for the single mineral dusts, oversized impingment cones were formed using a facility that allows for shooting a jet of dust laden air against a metal coupon. The mass of dust that deposited on each coupon was measured as well as the volume of the cone. These two values allow for calculating ρ_{dep} which then allows for calculating the packing factor using ρ_{mat} data from Table 3.1. The air was heated to 950K to try and match the blockage test conditions. A full description of this facility may be found in Bowen et al. [3].

Initial results seemed promising. Albite had an average packing factor of 0.32 while dolomite had an average packing factor of 0.47. Albite having a lower packing factor would indicate that its deposits are larger for the same amount of dust than dolomite deposits, which could have explained the higher BPG. When it was attempted to create impingment cones for the remaining dusts, however, the cones that were formed were too small for measuring the volume (see Figure 3.6). This was surprising because in the effusion plate tests all dusts did form deposits (although salt did have fairly small deposits even for the effusion plate tests). This suggested that maybe the impingement cones were formed under conditions that were not very similar to those seen in the effusion plate tests and that the packing factor estimates may not be relevant.

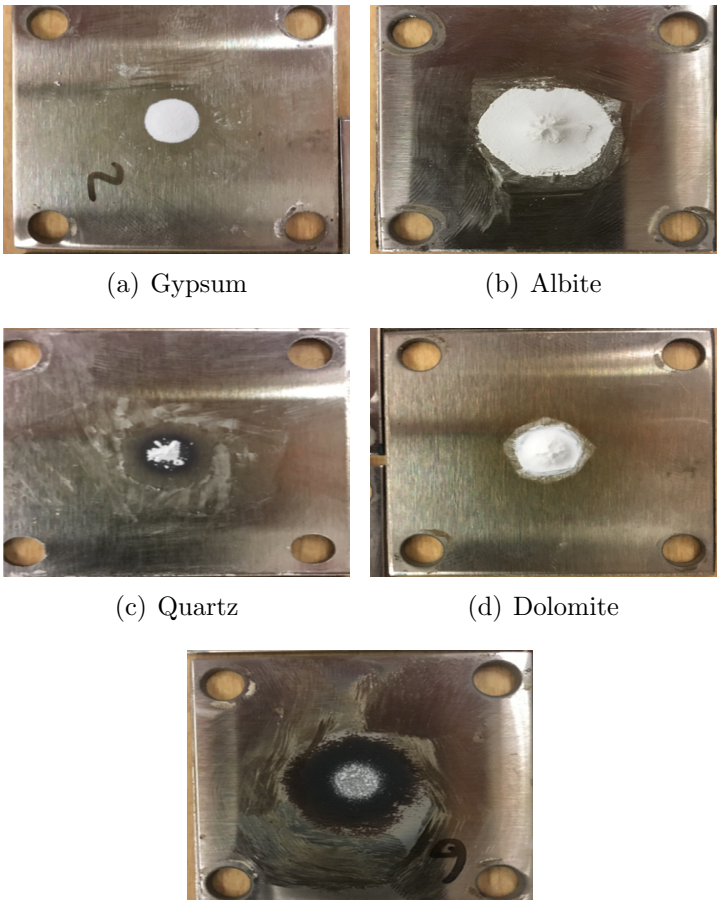

(a) Gypsum (b) Albite

(c) Quartz (d) Dolomite

(e) Salt

Figure 3.6: Impingement Cones

The flow in the effusion plate test fixture has been investigated via CFD by Wolff [23]. An image of the coolant velocity through the hole is shown in Figure 3.3.5. The coolant velocity is relatively low through the plenum portion of the test figure and doesn't reach velocities much higher than 20m/s until it enters the hole. Compared to the test facility used to form the impingement cones, which has a mean flow velocity of 86m/s at the exit of the pipe, the particles likely impacted the effusion hole wall at

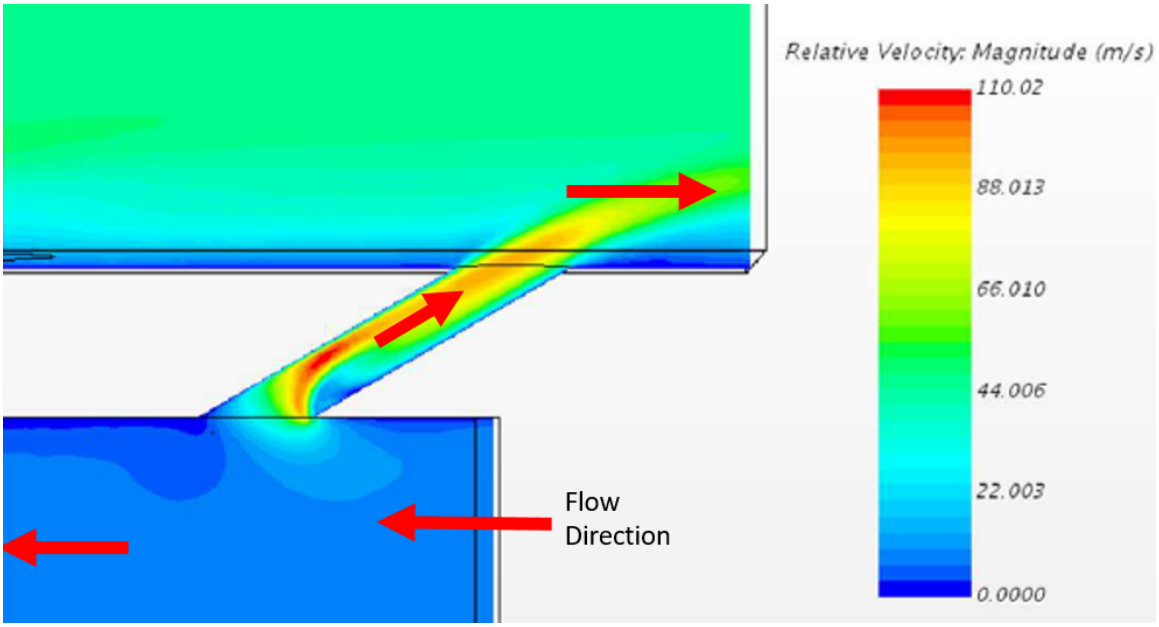

Figure 3.7: Flow Velocity throughout Effusion Hole. Note: Top of Image Represents Hole Outlet [23]

a lower velocity than they did the metal coupon. This may be one reason why such small cones were formed.

Another difference between the two test conditions was the temperature of the deposition surface. When forming the cones, the metal coupons were only heated by the jet of 950K air for a short duration before injecting dust, while the effusion plates are heated to an external surface temperature of 1116K

3.3.6 Melting and Sintering

So far in this discussion the effect of elevated dust temperatures has not yet been considered. Because the test facility is meant to simulate an internal cooling geometry, the temperatures are not extremely high, and widespread melting that may be experienced in the main gas path of an engine was not seen. When particles do

Table 3.6: Dust Melting Points [14][24]

Mineral	Melting Point (K)	Average BPG
Quartz	1983	54.2
Albite	1373	172
Gypsum*	2873	82.9
Dolomite*	2873	11.1
Salt	1075	7.6

begin to melt, they can splatter on engine hardware and form deposits. If in a mixture of dust one substance begins to melt, it can act as a catalyst to accelerate deposition.

The melting points for the single mineral dusts used are listed in Table 3.6. The asterisks indicate dusts which undergo a decomposition into different materials prior to melting. Gypsum will decompose into CaO at 1117K and dolomite will decompose into CaO and MgO at 873-1073K. Listed in Table 3.6 are the melting temperatures of the products of the decomposition.

While the melting points of all materials except salt are above the coolant and plate temperatures experienced during a test, sintering may occur at temperatures lower than the melting point. When this happens, the dust particles could soften and be more likely to adhere to the plate. This was seen by Opie who performed sintering tests using AFRL 02 at temperatures starting at 1273K. After being heated to 1273K, the AFRL 02 dust showed signs of sintering although still remained in a powdery form [13].

Due to the difficulty of finding information about the sintering behavior of mineral dusts in the literature, sintering tests were performed. The goal of this test was to explore the extent to which the dusts may or may not sinter at the temperature they

experience in a deposition test. First, the temperature on the inside of the plate was estimated to be 1105K by a 1-dimensional heat transfer analysis. This analysis did not consider any additional cooling that will be experienced as a result of the effusion holes so 1105K is likely an over estimated temperature. Next, small piles of dust were place on ceramic coupons. The piles were approximately 10mm in diameter and were sized to be large enough to observe but small enough to better represent the small deposits found in an effusion hole. The kiln was set so that the location of the kiln where the coupons would be placed was brought to 1105K and then the coupons were placed in the kiln through the view port on a sliding stand. The kiln remained at temperature for 30 minutes and then was shut off and cooled down while the dust samples remained on the sliding stand inside the kiln. This heating cycle was chosen to represent the conditions a dust particle experiences in a test because the time at temperature is an important parameter in melting reactions as well as the specific temperature.

To protect the test fixture from becoming too hot during this test, some air was supplied through the fixture. This air happened to locally change the temperature at certain points in the kiln, including where the samples were placed, so it was difficult to achieve the target temperature exactly. Figure 3.8 shows the actual temperatures seen during the sintering test. Figure 3.9 shows the thermocouple placement inside the kiln. The kiln thermocouple was placed close to the test fixture outlet so it measured a lower temperature. The kiln was kept at constant temperature for a half hour before being turned off.

Figure 3.3.6 shows images of the dust pre and post bake. The majority of the dusts did not experience much of a change during the test. Salt and albite are the exception.

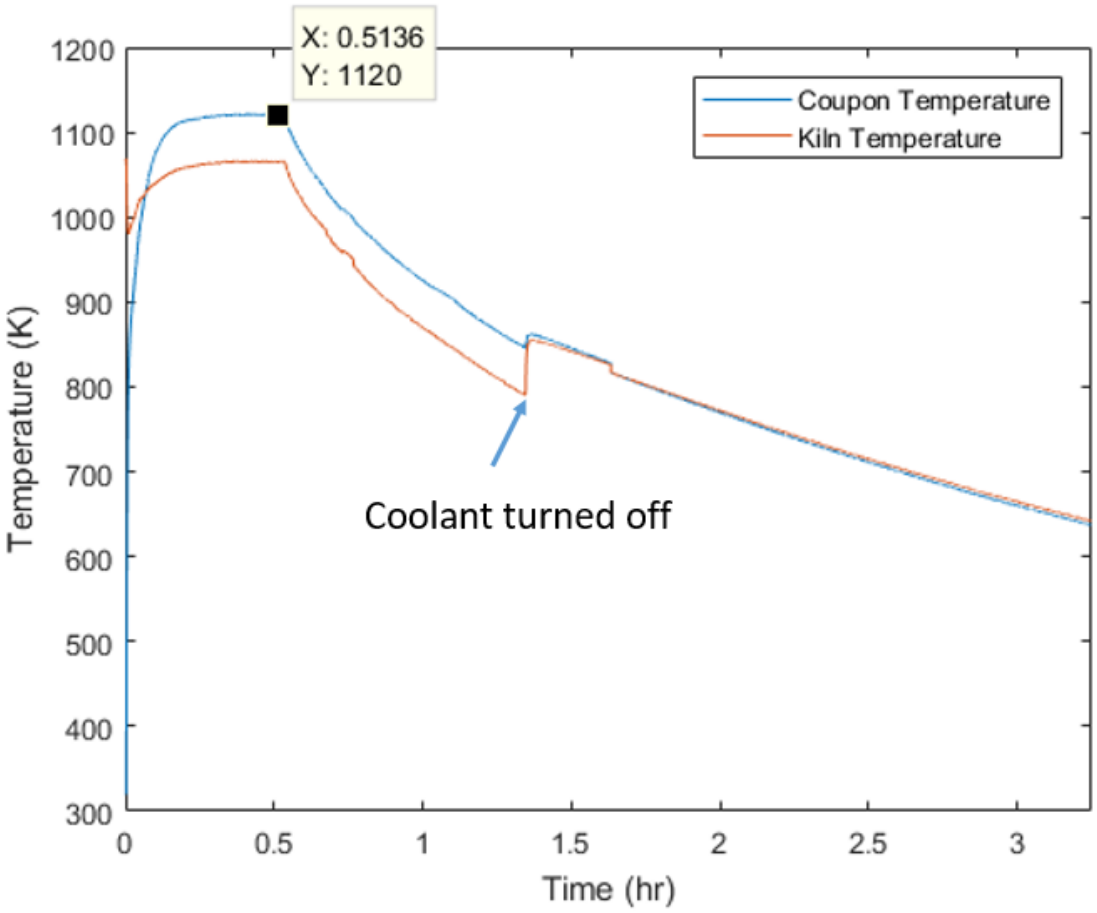

Figure 3.8: Temperatures During Sintering Test. Note: Data Logging Software Malfunctioned after 3.25 Hours

Salt appeared to have melted away during this test as it was no long present on the coupon after the bake. Molten NaCl at 1120K is slightly less viscous than water (about 0.96 mPa*s compared to 1.0 mPa*s for water at room temperature) so if it did melt it is possible that it would have dispersed across the coupon [10]. Albite appeared to have turned a slightly darker shade of tan than it had before the test. Albite has the second lowest melting point among the mineral dusts after salt (Table 3.6) so it would make sense if it sintered before the other dusts.

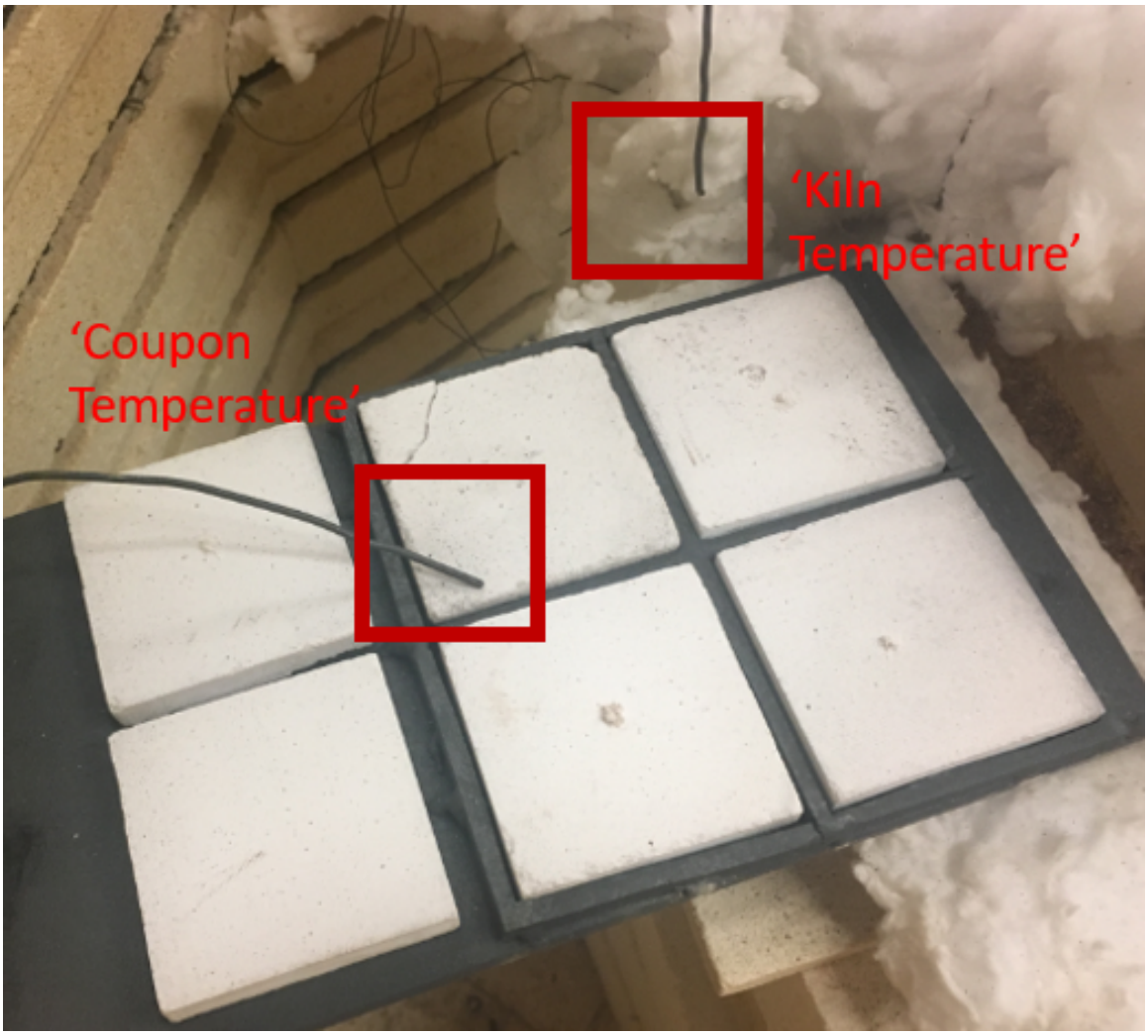

Figure 3.9: Thermocouple Placement inside the Kiln

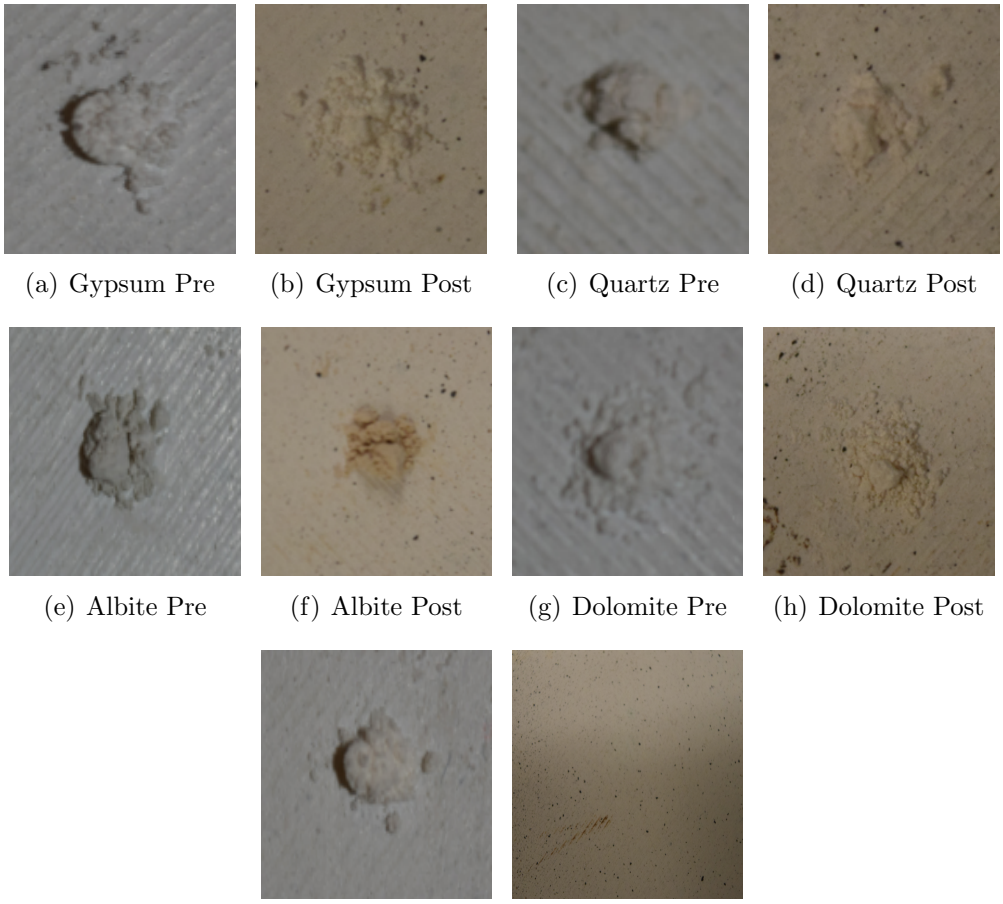

(a) Gypsum Pre (b) Gypsum Post (c) Quartz Pre (d) Quartz Post

(e) Albite Pre (f) Albite Post (g) Dolomite Pre (h) Dolomite Post

(i) Salt Pre (j) Salt post

Figure 3.10: Images of Dust Piles Pre and Post Bake

CHAPTER 4

Conclusions and Recomendations for Future Work

Experimental deposition tests were conducted to investigate the effects of dust composition in an internal cooling geometry. A dust's ability to form deposits that are detrimental to cooling mass flow is described by the mass flow reduction, (which corresponds to blocking of the effusion holes), divided by mass of particles injected into the facility. Even when controlling for size, dust composition is an important parameter that will influence how a dust deposits. The test results for the pure mineral dusts provide evidence for this: BPG varied for all five single mineral dusts. In searching for an explanation, material dependance, mechanical properties, adhesion forces, and melting temperatures, and sintering behaviors were explored although no obvious correlation could be made.

The five pure mineral dusts were combined in the same mass fraction as they are found in AFRL 02 and an attempt was made to predict the BPG for this mixture by taking a mass-weighted average BPG from the test results of the single mineral dust. The estimated BPG from the mass-weighted average exceeded the BPG of the OSU-mixed AFRL 02 dust, indicating that it is not accurate to predict the blocking behavior of a mixed dust in this way. The OSU-mixed AFRL 02 also had a lower BPG than the version of AFRL 02 that was created by milling AFRL 02 that was

already mixed in a larger size distribution. Because the size distributions of the individual constituents likely differ between these two dusts, this shows that not only is overall size distribution an important parameter but that the size distribution of individual constituents is also an important parameter in predicting deposition of non-homogeneous dust mixtures in effusion holes. In this case, albite may have had a smaller size distribution in the milled AFRL 02, causing a higher BPG.

In addition to the two previously mentioned AFRL 02 dusts, unmilled AFRL 02, which has a larger size distribution than both the milled and mixed AFRL 02 dusts, was also tested. This dusts had the lowest BPG among the AFRL 02 dusts. This result is consistent with the size dependency of deposition in effusion holes that was found in Wolff et al. [22].

There are a few additional tests that could provide useful information but could not be completed in time to include in this work. Testing of more mixtures of dust may provide insight into the specific interactions between the different minerals when they are depositing. A variation of AFRL 02 without dolomite may be expected to have a higher BPG. Dolomite was seen to form large deposits on the effusion hole and this may alter the streamlines into the hole. If the streamlines are altered in a way that causes particles to impact at higher velocity or shallower angle this may reduce deposition.

Salt had the lowest melting point among the dusts tested and was seen to melt in the sintering test. A variation of AFRL 02 where salt is removed may have a different BPG than mixed AFRL 02 even though it makes up a small portion of the dust. If the BPG is lower, salt could be acting as a catalyst for deposition when present in a mixture.

The QDGS blend had a lower BPG than the OSU-mixed AFRL 02, although the difference wasn't dramatic. The fraction of salt in the QDGS blend is almost twice as high as the fraction of salt present in AFRL 02. Testing another version of the QDGS blend could likely be better compared to AFRL 02.

Another area that was explored unsuccessfully was packing factors of the different dusts. Initial results were promising and seemed to indicate that the lower packing density of albite may be responsible for albite blocking the effusion holes so quickly. Other dusts failed to produce measureable cones however and it was decided that the cones were formed at conditions that were not relevant to what would be experienced in the effusion plate test section. An investigation into the shapes of the particles and how they pack together at lower velocities would provide insight to the role packing density played in this study.

BIBLIOGRAPHY

[1] Lennart Bergström. Hamaker constants of inorganic materials. *Advances in Colloid and Interface Science*, 70:125–169, 1997.

[2] J. P. Bons, R. Prenter, and S. Whitaker. A simple physics-based model for particle rebound and deposition in turbomachinery. *Volume 5B: Heat Transfer*, 2016.

[3] Christopher P Bowen, Nathan D Libertowski, Mehdi Mortazavi, and Jeffrey P Bons. Modeling deposition in turbine cooling passages with temperature-dependent adhesion and mesh morphing. *Journal of Engineering for Gas Turbines and Power*, 141(7):071010, 2019.

[4] R. Allen Bowling. *A Theoretical Review of Particle Adhesion*, chapter Particles on Surfaces 1: Detection, Adhesion, and Removal, pages 129–142. Springer US, Boston, MA, 1988.

[5] Michael G Dunn, Adam J Baran, and Jerry Miatech. Operation of gas turbine engines in volcanic ash clouds. *Journal of engineering for gas turbines and power*, 118(4):724–731, 1996.

[6] Said Elghobashi. On predicting particle-laden turbulent flows. *Applied scientific research*, 52(4):309–329, 1994.

[7] Johann P Engelbrecht, Eric V McDonald, John A Gillies, and Alan W Gertler. Final report for the department of defense: Enhanced particulate matter surveillance program, 2008. W9124R-05-C-0135/SUBCLIN 000101-ACRN-AB, Febuary 2008.

[8] David B Hough and Lee R White. The calculation of hamaker constants from liftshitz theory with applications to wetting phenomena. *Advances in Colloid and Interface Science*, 14(1):3–41, 1980.

[9] Jacob N Israelachvili. *Intermolecular and Surface Forces*. Academic Press, 2011.

[10] T Ito, N Kojima, and A Nagashima. Redetermination of the viscosity of molten NaCl at elevated temperatures. *International Journal of Thermophysics*, 10(4):819–831, 1989.

[11] Rhonda J Lee and L-S Fan. The effect of solid interaction forces on pneumatic handling of sorbent powders. *AIChE journal*, 39(6):1018–1029, 1993.

[12] Robert J Moffat. Describing the uncertainties in experimental results. *Experimental thermal and fluid science*, 1(1):3–17, 1988.

[13] Nathaniel P Opie. A comparison of afghanistan, yuma, az, and manufactured sands melted on eb-pvd thermal barrier coatings. Master's thesis, 2014.

[14] John Rumble. *CRC handbook of chemistry and physics*. CRC press, 2017.

[15] GR Salazar-Banda, MA Felicetti, JAS Gonçalves, JR Coury, and ML Aguiar. Determination of the adhesion force between particles and a flat surface, using the centrifuge technique. *Powder technology*, 173(2):107–117, 2007.

[16] James L Smialek, Frances A Archer, and Ralph G Garlick. Turbine airfoil degradation in the persian gulf war. *JOM*, 46(12):39–41, 1994.

[17] Wenjia Song, Yan Lavallée, Kai-Uwe Hess, Ulrich Kueppers, Corrado Cimarelli, and Donald B. Dingwell. Volcanic ash melting under conditions relevant to ash turbine interactions. *Nature Communications*, 7(1), 2016.

[18] William Murray Telford, WM Telford, LP Geldart, Robert E Sheriff, and RE Sheriff. *Applied Geophysics*, volume 1. Cambridge University Press, 1990.

[19] J Webb, B Casaday, B Barker, JP Bons, AD Gledhill, and NP Padture. Coal ash deposition on nozzle guide vanes—part I: Experimental characteristics of four coal ash types. *Journal of Turbomachinery*, 135(2):021033, 2013.

[20] W. E. West and J. W. Westwater. "Radiation-Conduction Correction for Temperature Measurements in Hot Gases". *Industrial and Engineering Chemistry*, 45(10):2152–2156, October 1953.

[21] Steven M Whitaker and Jeffrey P Bons. An improved particle impact model by accounting for rate of strain and stochastic rebound. In *ASME Turbo Expo 2018: Turbomachinery Technical Conference and Exposition*, pages V02DT47A016–V02DT47A016. American Society of Mechanical Engineers, 2018.

[22] Trent Wolff, Christopher Bowen, and Jeffrey P Bons. The effect of particle size on deposition in an effusion cooling geometry. In *2018 AIAA Aerospace Sciences Meeting*, page 0391, 2018.

[23] Trent M Wolff. The effect of particle size on deposition in an effusion cooling geometry. Master's thesis, The Ohio State University, 2018.

[24] Christopher A Wood, Sonya L Slater, Matthew Zonneveldt, John Thornton, Nicholas Armstrong, and Ross A Antoniou. Characterization of dirt, dust and volcanic ash: A study on the potential for gas turbine engine degradation. Technical report, DST-Group-TR-3367, 2017.